

Beyond the Local Volume: Surface Densities of Ultracool Dwarfs in Deep HST/WFC3 Parallel Fields

CHRISTIAN AGANZE,¹ ADAM J. BURGASSER,¹ MATHEW MALKAN,² CHIH-CHUN HSU,¹ CHRISTOPHER A. THEISSEN,¹ DANIELLA C. BARDALEZ GAGLIUFFI,³ RUSSEL RYAN,⁴ AND BENNE HOLWERDA⁵

¹*Department of Physics, University of California, San Diego, CA 92093, USA*

²*Department of Physics & Astronomy, University of California, Los Angeles, CA 90095, USA*

³*Department of Astrophysics, American Museum of Natural History, Central Park West at 79th Street, NY 10024, USA*

⁴*Space Telescope Science Institute, 3700 San Martin Dr., Baltimore, MD 21218*

⁵*Department of Physics and Astronomy, 102 Natural Science Building, University of Louisville, Louisville KY 40292, USA*

ABSTRACT

Ultracool dwarfs (UCDs) of the L, T, and Y spectral classes are the lowest-mass and coldest objects in the Milky Way. Like stars, they are tracers of Galactic structure and star-formation history, while the cooling of substellar UCDs provide additional probes for galactic archeology and chemical evolution. Wide-field optical and infrared surveys have uncovered thousands of UCDs, but primarily in the immediate solar neighborhood ($d < 100$ pc). To push to larger distances, we have searched over 0.5 deg^2 of the WFC3 Infrared Spectroscopic Parallel Survey and the 3D-HST parallel survey with low-resolution near-infrared spectra. We report the discovery of 168 M7-T9 and T dwarfs with spectro-photometric distances up to ~ 2 kpc for L dwarfs and ~ 400 pc for T dwarfs. We model the number density distribution with population simulations incorporating various assumptions of the intrinsic MF and birth rates, accounting for UCD evolutionary models and Galactic structure. We under-predict the number den-

sity of T dwarfs in our simulation, reflecting a larger scale height ($h > 1000$ pc) for these old populations. Future infrared sky surveys conducted with the James Webb Space Telescope (JWST) or the Euclid mission will put finer constraints on the true scale height of UCDS. We predict that Euclid will yield $\sim 10^4$ L dwarfs and $\sim 10^4$ T dwarfs spectra in the Euclid South and Euclid Fornax fields alone for a limiting magnitude of $J=24$, providing enough statistics to fully characterize UCDs in the Galactic context.

1. INTRODUCTION

The structure and evolution of the Milky Way is largely inferred from heterogeneous spatial and kinematic distributions of its stars. Star-count data show that the overall structure conforms to a younger population fit to one or more exponential disks and an older population fit to a power-law or oblate spheroid (de Vaucouleurs & Pence 1978; Bahcall & Soneira 1981; Jurić et al. 2008); and models show that the disk started forming stars 8–11 Gyr ago, while the halo star-formation history dates to 10–13 Gyr ago from possible multiple merger events. Hence, halo stellar populations contain stars with ages comparable to the age the universe (Leggett et al. 1998; Tolstoy et al. 2009; Haywood et al. 2013). Questions relating to the formation and evolution of the Galaxy through its stars constitute the field of Galactic archeology (Freeman 1987; Ivezić et al. 2012), which, through the usage of large sky surveys (e.g the Sloan Digital Sky Survey, York & Others 2000), has enabled a 6-dimensional depiction of the Galaxy. The Gaia mission (Gaia Collaboration et al. 2018) has recently contributed to our understanding of the Milky Way. Some of the notable discoveries include major merger events that formed the inner stellar halo and thick disk (Gaia-Enceladus/Gaia sausage: Helmi et al. 2018; Belokurov et al. 2018; Myeong et al. 2018; Gallart et al. 2019, and the Sequoia event: Myeong et al. 2018, 2019), the discovery and characterization of hypervelocity stars (Boubert et al. 2018), stellar streams as probes of the Galactic potential and dark matter profile (Boubert et al. 2018; Malhan et al. 2018; Koppelman et al. 2019). The Gaia mission has also enabled the discovery of substructure in the solar neighborhood in the galactic disk caused by phase mixing in velocity space, from possible interactions with the spiral structure of the Galaxy (Antoja et al. 2018).

Ultracool dwarfs (UCDs; $M \lesssim 0.1 M_{\odot}$, $T_{eff} \lesssim 3000\text{K}$; Kirkpatrick 2005) provide a new approach for studying the Galaxy (Burgasser 2004; Ryan et al. 2017). They constitute $\sim 50\%$ of the total number of stars and they are abundant in every environment in the Galaxy (Cruz et al. 2007; Chabrier & Baraffe 2000; Burrows et al. 2001; Bochanski et al. 2010). Stellar UCDs have lifetimes far in excess of the age of the Galaxy ($> 10^3$ Gyr, Laughlin et al. 1997), while substellar UCDs (brown dwarfs) do not fuse hydrogen and hence cool down with time (Hayashi & Nakano 1963). They have distinct spectra shaped by strong molecular absorption bands that are highly sensitive to temperature, surface gravity and metallicity. The evolution of UCDs provides potential age diagnostics that have already been exploited in stellar cluster studies (Basri 1998; Luhman & Mamajek 2012; Martin et al. 2017) and searches of young moving groups near the Sun (Lopez-Santiago et al. 2006, Gagné et al. 2015, Mamajek 2015, Faherty et al. 2018).

UCDs have historically been discovered in red optical and infrared sky surveys (DENIS: Delfosse et al. 1999, SDSS: Schmidt et al. 2010, 2014; Theissen et al. 2017, VISTA: Lodieu et al. 2012; Downes et al. 2014; 2MASS: Cruz et al. 2007; Kirkpatrick et al. 2010, WISE: Kirkpatrick et al. 2011; Cushing et al. 2011, UKIDSS: Marocco et al. 2015; Day-Jones et al. 2013; Burningham et al. 2013; Skrzypek et al. 2016, CFHT-LAS: Reyle et al. 2010, Gaia: Reylé 2018; Kiman et al. 2019) but due to their intrinsic faintness, these samples are distance limited ($\leq 100\text{pc}$). Hence, efforts to measure the UCD luminosity function have focused on compiling volume-limited samples within 20–25 pc of the sun (Cruz et al. 2007; Metchev et al. 2008; Reyle et al. 2010; Kirkpatrick et al. 2019; Bardalez Gagliuffi et al. 2019). Wide-field surveys provide large samples of UCDs, however, these studies do not effectively probe Galactic structure, nor the oldest UCD populations that formed in the early metal-poor Galaxy which may have had a distinct initial mass function (Bate et al. 2002; Bromm & Loeb 2003; Bate et al. 2003). To investigate the complete UCD population of the Galaxy these scenarios, it is necessary to identify UCDs populations beyond the solar neighborhood and further into the thick disk and halo of the Milky Way.

Deep pencil-beam imaging surveys provide a novel approach to use star-count data in characterization of UCD populations beyond the local volume. A common approach is to use photometric

selections cuts anchored to known sample. Early work by [Gould et al. \(1997\)](#) conducted an M-dwarf number counts to measure the halo luminosity function of the Hubble Space Telescope’s Wide Field Camera 2 (HST-WFC2) and Planetary Camera (PC1) Deep Fields. They found 47 M dwarfs with $M_V > 13.5$, and the distribution was consistent with a power law the mass function that turns at $M \sim 0.6 M_\odot$ from $\alpha = -1$ to $\alpha = 0.44$. Subsequent studies by [Kerins \(1997\)](#); [Chabrier & Mera \(1997\)](#) concluded that the contribution of low-mass stars ($M \sim 0.3 M_\odot$) to the halo luminosity function is less than 1%. [Ryan Jr. et al. \(2005\)](#) searched 15 deep parallel fields from the Hubble Space Telescope star-count optical data obtained with the ACS instrument, selected by their i-z colors. They estimated a scale of ~ 350 pc for L & T dwarfs. Later work by [Ryan et al. \(2011\)](#) found 17 late M, L and T dwarfs in 231.90 arcmin^2 of WFC3 imaging of the GOODS fields using a combination of wide and narrow-band filter colors. They estimated a disk scale height of 290 ± 39 pc consistent with work by [Pirzkal et al. \(2005\)](#). In addition to poor estimate of spectral types, these samples were contaminated with various non-stellar sources that could not be identified in the absence of spectral information. To push towards a larger and pure sample, [Holwerda et al. \(2014\)](#) identified 274 in 227 arcmin^2 M-dwarfs (to a limiting magnitude F125W=25) from the HST-WFC3 Brightest of Re-ionizing Galaxies (BoRG, [Pirzkal et al. 2009](#)) survey, using an optical and near-infrared colors and determined their spectral types using V-J color-M-dwarf subtype relation ([Pirzkal et al. 2009](#)). They found a slightly higher density of M-dwarfs identified in the Northern fields compared to the Southern Fields, and a disk scale-height of 0.3–4 kpc with a dependence on subtype. The overall M-dwarf scale height was ~ 600 pc, a number that is much larger than previous estimates mostly due to large uncertainties in the fit. [Van Vledder et al. \(2016\)](#) reanalyzed these data using a Markov Chain Monte Carlo method to fit the statistic to a galactic model including a thin disk, thick disk, and halo component. They derived a scale height of 290_{-19}^{+20} pc and a central number density of $0.29_{-0.13}^{+0.20} \text{ pc}^{-3}$, with no correlation of model parameters with M-dwarf subtype, and consistent with previous studies. However, these studies do not probe statistics for later types. Recent work by [Sorahana et al. \(2018\)](#) found 3665 L dwarfs brighter than $z=24$ by searching 130 square degrees of the Hyper Suprime-Cam Subaru Strategic Program data and found an average L-dwarf scale height of 340–420 pc. [Carnero](#)

Rosell et al. (2019) compiled a list of 11,745 photometrically classified L0-T9 dwarfs distances up to ~ 400 pc by searching $\sim 2,400$ deg 2 of the Dark Energy Survey (DES) data at a limiting magnitude of $z=22$. They estimated a large scale height of ~ 450 pc. These last two studies provide another constraint on the number density of L dwarfs in the Galaxy using large samples ($N > 10^3$); however, as in many imaging surveys, poor accuracy in spectral types significantly affects the derived parameters. Ultimately, the large uncertainties on spectral types of UCDs in imaging surveys poorly constrain their distances, and deep spectroscopic follow-up of these sources is not a priority for precious HST time.

A parallel approach is to use deep pencil beam samples of spectra in red optical and near infrared (NIR) with no prior selection of source type. NIR spectroscopy, in particular, samples the peak of UCD spectral energy distributions and measure broad molecular features that guide UCD classification schemes (Kirkpatrick 2005). Pirzkal et al. (2005) identified 18 late M and 2 L dwarfs in the Hubble Ultra Deep Field (HUDF) and estimated their spectral types by fitting templates from Kirkpatrick et al. (2000) to their Gradient-Assisted Photon Echo Spectroscopy (GRAPES, ref) taken with the xxx instrument (ref). This study inferred a disk scale height of 400 ± 100 pc for M and L dwarfs. Another study by Pirzkal et al. (2009) used deep Advanced Camera for Surveys (ACS) slitless grism observations of the Probing Evolution And Reionization Spectroscopically (PEARS) fields (as part the Great Observatories Origins Deep Survey (GOODS) fields, Giavalisco et al. 2004) down to a $z=25$ and spectroscopically identified 43 M4-M9 dwarfs. Using a thick and thin disk model, the study estimated a scale height for the thin disk of ~ 370 pc, and ~ 100 pc for the thick disk, a halo fraction between 0.00025–0.0005 consistent with previous estimates.

Masters et al. 2012 discovered 3 late T dwarfs the WFC3 infrared Spectroscopic Survey (WISPS) fields (Atek et al. 2010) identified by their strong CH₄ and H₂O absorption features. The sample size was not large enough to put meaningful constraints on the scale height or the luminosity function L and T dwarfs beyond the local volume. In this paper, we expand upon this study by developing an effective method to select UCDs in similar surveys.

Section 2 describes the data, section 3 describes the selection process, section 4 discusses the result compared to a Monte-Carlo simulation

2. DATA

We obtained data from two surveys: the WFC3 Infrared Spectroscopic Parallel Survey (WISPS, Atek et al. 2010) and 3D-HST (Momcheva et al. 2016, Brammer et al. 2012a, Skelton et al. 2014). These two surveys used the IR channel of the WFC3 camera (Kimble et al. 2008) providing low-resolution G102 ($\lambda = 0.8\text{--}1.17 \mu\text{m}$, $R \sim 210$) and G141 ($\lambda = 1.11\text{--}1.67 \mu\text{m}$, $R \sim 130$) grism spectra. Removal of the slit mask allows for the overlapping spectra of the 136×123 arcsec inner FOV of the WFC3 camera. Figure ?? shows an WCF3 exposure of one of fields in WISP.

2.1. 3D-HST survey data

3D-HST a parallel survey of 248-orbits spanning ~ 600 arcmin 2 as part of Hubble Cycles 18 & 19. This survey targets four standard deep extra-galactic fields: The All-wavelength Extended Groth Strip International Survey (AEGIS, Davis et al. 2007), Cosmic Evolution Survey (COSMOS, Scoville et al. 2007), Ultra-Deep Survey(UKIDSS-UDS, Lawrence & Others 2007), the Great Observatories Origins Deep Survey (GOODS-South and GOODS-North, Giavalisco et al. 2004), using the ACS/G800L and WFC3/G141 grisms in parallel. The goal of 3D-HST is to obtain as the the Cosmic Assembly Near-infrared Deep Extragalactic Legacy Survey(CANDELS survey, Grogin et al. 2011, Koekemoer et al. 2011. However, 3D-HST is only 70% of the total footprint of the CANDELS. Photometric catalog data products are described in Skelton et al. (2014) and combined data products in Momcheva et al. (2016)

The pointings for 3D-HST are designed to cover CANDELS area, therefore there are additional ground-based and space-based photometry from various other surveys in several optical and infrared filters. Each pointing in 3D-HST is observed by two orbits using the G141 grism and the F140W filter with typical exposure times of 5000 s for G141 AND 800 s for F140W. Observations for most of the pointings in the survey were conducted from October 2010 to November 2012. However, the GOODS-North field is a part of the A Grism H-Alpha SpecTroscopic survey (AGHAST, GO-11600;

PI: Wiener) and was observed between sept 16 2009 and sept 26 2010 and re-observed on April 19 and 24 2011, due artifacts and background issue, with exposure times of 800 s for F140W AND 5200S in G141.

Data reduction in 3D-HST involves reducing the both the direct F140W images and G141 grism images. The full description of the image reduction pipeline is described by Brammer et al. (2012b), Skelton et al. (2014) and Momcheva et al. (2016). Raw images were downloaded and passed through a pipeline that consists of removing satellite trails and artifacts through visual inspection, background -subtraction and flat-fielding. The main physical sources of time-dependent background are zodiacal continuum, scattered light and persistence from He emission at 1.083 micron. Both the reduction of the F140W and G141 images involved combining at most four dithered images. A standard method uses a drizzling algorithm implemented by the AXe software (Kuntschner et al. 2013; Kümmel et al. 2009). However, drizzling is designed to work well for a large number of images. The shortcomings of this method include the introduction of correlated noise between adjacent pixels. To avoid these issues, 3D-HST stacked all the dithered images onto one grid, given that the dithered images are all separated by the same number of pixels by the design of the survey. In addition, reducing the grism images require a reference image (different from the obtained F140W direct image) to generate a contamination global model of each pointing, to separate overlapping spectra and orders. The reference image was obtained by coming F125W, F140W AND F160W images of that pointing obtained from Skelton et al. (2014) data products, where the magnitudes of all objects in the fields are scaled to the F140W zero-point, and errors properly propagated. Based on the morphology and the magnitude of each source in the reference image, the full 2D-spectrum of each object was modeled from a 1D SED. This contamination model was then used to correct for overlapping spectra and orders. These 2D-spectra of exactly 312 pixels each are then extracted. The reference image and the direct images are on the same grid, therefore no source matching was required for source identification.

We used data products described by Momcheva et al. (2016) and the photometric catalog of sources in Skelton et al. (2014) retrieved from the survey’s website ¹. The extracted 1D spectra in 3D-HST survey are not continuum-corrected as shown in Figure 6. We obtained a correct continuum of each 3D-SHT spectrum by dividing the flux of the spectrum and the sensitivity curve of the detector provided in the data. We did not perform any additional reduction to the data.

2.2. *WISP survey data*

The WISP survey is a 1000-orbit HST pure-parallel survey covering 390 fields ($\sim 1500 \text{ arcmin}^2$) that follows observing programs accepted on the Cosmic Origins Spectrograph (COS) and Space Telescope Imaging Spectrograph (STIS). The survey’s observing strategy as well as data-reduction is described in Atek et al. (2010). The goal of WISPS is to conduct a census of star-forming high-redshift galaxies. The fields in WISPS were chosen away from the galactic plane and 5.5 and 4.75 arcmin away from the fields of COS and STSIS. Given the pure-parallel nature of this survey, the fields are observed in G102, G141 grism with no dithering between exposure. Reference images were also taken using F110W (corresponding to G102) and F140W (corresponding to G141) imaging cameras. To reach the same depth in both G102 and G141, the ratio of exposure times was fixed at 2.4:1, while the exposure ratio of exposure times for imaging and grism is 6:1.

Data reduction and grism extraction was performed using a combination of **AXe** software (Kuntschner et al. 2013; Kümmel et al. 2009) and custom IDL pipelines to remove additional background and to flag bad pixels. The main sources of background are zodiacal light, and earth thermal emissions. Grisms spectra in WISPS have little crowding of the same fields given their high galactic latitudes, but multiple spectral orders do overlap. WISPS provides an estimate of contamination of each spectrum computed using **AXe** and source catalogs in WISPS were generated using SExtractor (Bertin & Arnouts 1996). We obtained WISPS G102 and G141 grism data as well as broad-band

¹ <https://3dhst.research.yale.edu/Home.html>

F110W, F140W, F160W photometric data and source catalogs from the Mukuliski Archive for Space Telescope (MAST^{[2](#)}).

2.3. *Reduced Data Products*

3. SELECTION OF UCDS

3.1. *Calibration Samples*

To find a sample of UCDs in WISPS & 3D-HST data, we created a calibration sample of known UCDs, with similar features, e.g spectral coverage and resolution to define our selection methods and quantity their efficiencies and biases. We obtained 2056 M7-T9 low-resolution (\sim 75-120), NIR (0.9-2.5 μ m) spectra of nearby brown dwarfs with median SNR >10 from the SpeX Prism Library (SPL, Burgasser 2014a, https://cass.ucsd.edu/~ajb/brown_dwarfs/spexprism/library.html) of UCDs. We will refer to this sample as the templates/SpEX sample. In addition, we compiled a list other UCD spectra taken with the same instrument. We used the 77 UCDs from Manjavacas et al. (2018) observed with the WFC3 as part of a study of cloud properties of hot Jupiters and brown dwarf atmospheres and compilation of a WFC3 UCD library. The Schneider dataset is a list of 22 Y dwarfs obtained by Schneider et al. (2015) using the WFC3 camera with the same resolution and wavelength coverage. These objects were targeted as a part of a program to determine spectroscopic markers of the T/Y dwarf transition. We combined these three sets of spectra.

3.2. *Pre-selection*

3.2.1. *Point-source Cut*

We combined all grism data and photometry from both surveys and obtained a total of 271915 grisms that have corresponding photometry in the provided photometric catalogs. To narrow down our selection, point sources were identified using `Source Extractor`'s stellarity index `CLASS_STAR` $\neq 0$. 3D-HST provides an additional `star_flag` flag for point-sources based on their F160W magnitudes and the flag `FLUX_RADIUS`, but we find that this flag eliminates 3 UCDs from 3D-HST in the selected

² <https://archive.stsci.edu/prepds/wisp/>

sample of UCDs, hence the flag was ignored. We reduced the sample down to 110930 spectra, that is 40.7% of the total number of spectra.

3.2.2. *J-band SNR rejection*

UCDs display a strong H₂O and CH₄ absorption features in the J and H bands. We do not expect other objects in this survey to display similar molecular broad features, hence to narrow down our selection, we defined a signal-to-noise ratio in the J-band continuum (hereafter J-SNR) in the wavelength region of 1.2 μm ≤ λ ≤ 1.3 μm. This J-SNR captures the amount of flux in the J-band, hence we eliminated the lowest SNR objects by making a cut at J-SNR = 3 retaining 46370 spectra/grisms, that is 38.7 % of the original point-source sample and 15.8% of the total number of spectra. We also measured the J-SNR for all the spectra in our calibration samples in a similar fashion.

3.3. *Spectral Fitting and F-test*

After the J-SNR cut, we fitted spectra to UCDs SpeX spectra of spectral standards using a χ² minimization method, following the method of Kirkpatrick et al. (2010). We obtained a spectral type classification all available WISP and 3D-HST spectra. We also compared every spectrum to a straight line in the same wavelength region and measured χ². These two fits help distinguish between spectra that could potentially have absorption features in this region, and spectra that have no interesting features and/or noisy spectra in this wavelength region. The χ² of a line (χ_L^2) or a standard (χ_T^2) is given by

$$\chi_L^2 = \sum_{\lambda=1.15\mu\text{m}}^{1.65\mu\text{m}} \frac{(a + b\lambda - \text{Sp})^2}{\sigma^2} \quad (1)$$

$$\chi_T^2 = \sum_{\lambda=1.15\mu\text{m}}^{1.65\mu\text{m}} \frac{(\text{Sp} - \alpha T)^2}{\sigma^2} \quad (2)$$

α is scale-factor defined as

$$\alpha = \sum_{\lambda=1.15\mu\text{m}}^{1.65\mu\text{m}} \frac{(\text{Sp} - \alpha T)^2}{\frac{T^2}{\sigma^2}} \quad (3)$$

$\text{Sp}(\lambda)$ is a WISP or 3D-HST spectrum and σ^2 is the noise in the WISP or 3D-HST spectrum a and b are the parameters of the best-fit line from least-squares and T is the template.

We then use an F-test as a statistical hypothesis testing static to separate noisy/linear spectra from the rest of the sample implemented by Scipy [Jones et al. 2001](#)– as `scipy.stats.f.cdf`. A flat spectrum is defined as having $F(\chi_s^2/\chi_l^2) < 0.4$ meaning that the probability of the standard being a better fit to the spectrum than a line is <than 40%. This cut yields only 8148 objects, that is 18.9% of point-sources with $J\text{-SNR} > 3$, 7.3% of all point-sources and 3% of the original number of spectra we obtained from both surveys. These three steps eliminated most of the noisy contaminants.

3.4. Spectral Indices

After eliminating noisy and possible extra-galactic contaminants, we narrowed down the selection to true UCDs. UCDs display strong CH₄ and H₂O molecular features in $1.1 \mu\text{m} < \lambda < 1.7 \mu\text{m}$ region ([Burgasser 2001](#)), they can be separated from other stellar/galaxy populations using these features. Spectral Indices have traditionally been used to determine spectral types ([Tokunaga & Kobayashi 1999](#), [Cushing et al. 2000](#), [Allers et al. 2007](#), [Burgasser et al. 2007](#)). Thus, we defined spectral indices in five wavelength bands: 1.15–1.20 μm , 1.246–1.295 μm , 1.38–1.43 μm , 1.56–1.61 μm , or 1.62–1.67 μm ; denoted by H₂O-1, J-Cont, H₂O-1, H-Cont, and CH₄ respectively. Each index is the ratio of the median flux in these bands and the uncertainties for each index are estimated by random sampling, assuming these uncertainties are Gaussian-distributed. The index is given by

$$\text{Index} = \frac{\langle F(\lambda_1 < \lambda < \lambda_2) \rangle}{\langle F(\lambda_1 < \lambda < \lambda_2) \rangle} \quad (4)$$

, where at each wavelength i, we draw fluxes normally distributed according to the noise in the spectrum:

$$\{F(\lambda_i)\} \sim \text{Normal}(\langle F(\lambda_i) \rangle, \sigma(\lambda_i)) \quad (5)$$

. $\sigma(\lambda_i)$) is the noise at that wavelength, and $\langle F(\lambda_i) \rangle$ is the flux at that wavelength.

We defined selection criteria using boxes/parallelograms in each of 45 independent, index-spectral index spaces. We expect UCDs with similar spectral types to cluster or follow a linear trend, away from the contaminants while the evolution of the relative strength H₂O and CH₄ bands with subtype

should distinguish classes. We chose the following subtypes given their similarities : M7-L0, L0-L5, L5-L0, T0-T5, T5-T9, Y dwarfs and subdwarfs, however, these distinction need not be as rigid.

To define the parameters of each selection criterion/box, we fitted a characteristic line to each index pair (x-index, y-index) within a subtype, defining the slope/direction of the box: $y = m \times x\text{-index} + b$. Each box has four vertices (v_1, v_2, v_3, v_4) computed as $(x_{\max}, x_{\min}) = \text{median}(x\text{-index}) \pm 3 \times \text{std}(x\text{-index})$. On the x-axis, if x_{\max} is greater than the maximum of x-index, or if x_{\min} is less than the minimum of the x-index, i.e the box extends beyond the subtype, we set x_{\min} and x_{\max} and the minimum and maximum of x-index respectively. The extent of the boxes on the y-axis are determined by $(y_{\max}, y_{\min}) = m \times (x_{\max}, x_{\min}) + b \pm 0.4 \times dy$, where dy is the range of y-index ($\text{max}(y\text{-index}) - \text{min}(y\text{-index})$). From these values, we define $v_1 = (x_{\min}, y_{\max})$, $v_2 = (x_{\min}, y_{\min})$, $v_3 = (x_{\max}, y_{\max})$, $v_4 = (x_{\max}, y_{\min})$. These boxes are designed to enclose most of the objects in each subtype and to avoid outliers. We used rectangular boxes, for their simplicity, and low-contaminations for subtypes M7-L0, L0-L5, L5-T0, and Y dwarfs, where the vertices were determined in the same manner but with $m=0$ and $b = \text{median}(y\text{-index})$.

To assess the effectiveness of this method, we defined a completeness and a contamination statistic for each of the subtype group as follows:

$$CP = \frac{TEMP_s}{TEMP_{tot}} \quad (6)$$

$$CT = \frac{WFC3_s}{WFC3_{tot}} \quad (7)$$

where $TEMP_s$ is the number of templates selected by the box, $TEMP_{tot}$ is the total number of SpeX templates, $WFC3_s$ is the number of WISPS and/or 3D-HST spectra selected by the box, $WFC3_{tot} = 8148$ is the total of spectra. We only employed criteria with the lowest contamination and highest completeness to select UCDs. The best criteria for each of the subtype groupings are those with less than 1% contamination (except for subdwarfs) and with >90% completeness; they are summarized in Table 1.

As a naming convention, each criteria is named by the ratio of indices on the x-axis and the ratio of fluxes on the y-axis. The best selection criteria are the following for each subtype are: H₂O-1/J-Cont H₂O-2/H₂O-1 for the subtype of L0-L5 sensitive to the H₂O absorption feature in the J-band; H₂O-1/J-Cont CH₄/H-Cont for the L5-T0 sampling the relative ratio of H₂O and CH₄ features; H₂O-1/J-Cont CH₄/H₂O-1 for the M7-L0 subtypes, sensitive to the H₂O in the J-band and CH₄ features; H₂O-2/J-Cont CH₄/H-Cont for the T0-T5 subtypes, sensitive to the H₂O and CH₄ in the H-band; H-cont/H₂O-1 CH₄/J-Cont for the T5-T9 subtypes, sensitive to H₂O and CH₄. We use the index CH₄/H₂O-1 H₂O-2/J-Cont to select Y dwarfs from the Schneider sample and H₂O-1/J-Cont CH₄/J-Cont for the subdwarfs in the SpeX sample. In total, we selected 2910 spectra out of 8148. The large number comes from high contaminations for the M7-L0 and subdwarf boxes.

As a final step, after all selection has been applied, we visually inspected all the candidates UCDs to confirm their spectral type, and to remove missed outliers. We estimated the false positive rates for our methods after visual inspection and characterization of the UCDS. The false positive rate (FP) is given by

$$FP = 1 - \frac{WFC3_{true}}{WFC3_s} \quad (8)$$

where WFC3_{true} is the total number of objects that are in the spectral type range, and that are true UCDs. Our best selection criteria have FPs >90% which is to be expected given the number of true UCDs is much smaller than the number of spectra. Nevertheless, the number of spectra targeted for visual contamination have been down-selected from more than 200000 to ~ 3000 .

3.5. Random Forest Classifier

As an alternative to using selection boxes in 2D-space, we trained a random forest classifier by deploying `RandomForestClassifier` implementation by `scikit-learn` (Pedregosa et al. 2012) to classify potential UCDs in both surveys. Random forests have been shown to reliably predict M-dwarf subtypes based on colors (Hardegree-Ullman et al. 2019) analogous to spectral indices. In addition, random forests have been proven to perform star-galaxy classification in transient surveys, using photometry alone (Miller et al. 2017). Random forest algorithms use a set of independent

decision trees constructed based on a random set of features, they assign a final label by averaging the classifications obtained by each decision tree. Furthermore, random forests are a reliable method used to obtain classification for large datasets, given that the algorithm is relatively fast, unbiased by noisy features and easy to implement.

The training set of 11019 objects is composed of 8283 visually confirmed non-UCDs from several iteration of the box-selection method in the previous section, 77 objects from the Manjavacas set, 22 objects form the Schneider set. We labeled these sources using two labels: UCDs, which are objects with spectral types $\geq M7$, and non-UCDs which are objects with spectral types $\leq M7$ and/or part of the visually confirmed as non-UCDs. his labeling results in 2148 objects labeled as UCDs (label=1) 8871 and with label=0.

Choosing an appropriate set of features is an important part of designing a good machine learning classifier. By intuition, spectral indices, although they are correlated, are a good set of features to use. We added the signal-to-noise ratio in the J-continuum, the two χ^2 s and their ratio, and the F-test value as additional features. For missing features, we replaced those values with -99999.9 and scaled all features in the range [0, 1] using `MinMaxScaler`. To test the accuracy of our classifier, we use a procedure similar to that of ([Miller et al. 2017](#)). We used 2-fold cross validation score and split the training by 50% and 50% partitions. We computed the accuracy by starting with one index as a feature and then adding additional features. We tracked the accuracy of the classification using cross-validation (CV) scores for each additional feature. With only one spectral index, we achieved a classification score of 75.4%, with all additional features we achieved a CV score of 99.4 %, for which spectral indices were responsible for spectral indices alone were responsible for CV score up to 96.5%. We deployed the classifier on 26370 point-source objects in both surveys with $J\text{-SNR} > 3$, classifying 404 sources as UCDs with their spectral classification of $\geq M7$. We then visually inspected these objects and we found 136 to be real UCDs.

3.6. *Sample Characterization*

3.6.1. *M dwarfs*

We found 99 objects with speCtral types of M7-L0.

3.6.2. *Robust L & T dwarfs*

WISP L dwarfs—We identified x early (L0-L5) L dwarfs in WISP. WISP 0927+6027 is an L0 dwarf at ~ 320 pc discovered in the Par21 pointing of the WISPS survey. It has an apparent magnitude of F140W=18.6 and fits to the L0 dwarf standard with good agreement except for the wavelength ranges of 1.35 to 1.5 μm and 1.65 to 1.7 μm due to a possible underestimation or overcorrection of the contamination in those wavelength regions. WISP 1429+3224 is classified as an L0 at ~ 1.5 kpc discovered in the Par378 pointing of the WISP survey. Its apparent magnitude is F140W=22.4 and it has a low SNR (J-SNR=8). Major H₂O strength defining that spectral class are present in the spectrum despite the rise in noise in certain parts of the spectrum. The apparently visual companion is not a UCD, and was not selected by our methods. WISP 1605+1447 is an L0 dwarf at ~ 1.5 kpc found in the Par240 field of the WISP survey. The fit to the standard is relatively poor, and there is a ramp-up of signal $\lambda 1.6 \mu\text{m}$, a typical feature in WISP spectra due to a less-precise estimation of the background. WISP 1004+5258 is an L1 dwarf at ~ 1.8 kpc found in the Par438 field/pointing of the WISP survey. There is a puzzling extra flux at 1.3 micron. This object might not be a UCD. WISP 0246-0104 is an L1 dwarf at ~ 1.5 kpc in the Par438 pointing of WISPS. It is a noisier spectrum, but with major features offering a good fit to the standard. WISP 1150-2033 is classified as L1 at ~ 380 pc. It is a bright detection (F160W= 19.2) with a high SNR (J-SNR = 57). It's a good fit to the standard. WISP 0015-7955 is classified as L1 ~ 1.5 kpc in the Par244 pointing. It is a faint source with a J-SNR of 6 and F140W=22.2 but a relatively good fit to the standard. WISP 1618+3340 is another bright L dwarf in WISPS. It has an apparent magnitude of F110W =21.7 putting it at a distance of ~ 1 kpc. WISP 1133+0328 an L1 at ~ 1 kpc with F140W=22.0 with no particular interesting features. WISP 1154+1941 is an L1 ~ 1 kpc in a Par338. The spectrum shows a ramp-up in flux at longer wavelength, a common feature in WISP data.

WISP 1124+4202 is the only late L dwarf in WISPS. Its G141 spectrum with J-SNR =11 is in a good agreement with the SpeX spectral standard. The object has an F160W=21.5 and an estimated distance of ~ 650 pc.

3D-HST L dwarfs—For early dwarfs, L1 GOODSS 0333-2751, a bright detection at ~ 1.1 kpc with a brightness of F140W=21.4 and a J-SNR of 34. The G141 spectrum fits well to the standard except for the region $\lambda \in [1.3, 1.4] \mu\text{m}$. However, there is no visible contamination in the spectrum at that specific region, the poor fit might be attributed to the telluric correction. UDS 0217-0509 is an L1 dwarf in UDS-25, a nearly perfect fit to the standard. GOODSN 1236+6211 is an L2 dwarf in GOODSN-33 with a J-SNR of 12. The object is in close angular separation with other extra galactic contaminants, but the its spectrum has very little contamination. GOODSN 1236+6209 is a low-SNR detection (J-SNR = 5) classified as L2 at ~ 4 kpc in the GOODSN-34 pointing. This object is the farthest early L dwarf in the sample.

WISP T dwarfs—There are only x early T dwarfs from WISPS in the sample. WISP 1003+2854 is classified as T0 at ~ 1 kpc. The G141 spectrum displays deep H₂O and CH₄ features with a J-SNR of 6. The spectrum is a poor fit to the standard in noisy regions. The object has a magnitude of F160W=23.1 placing it at ~ 1 kpc. WISP 0437-1106 is another robust identification, classified as T3 and with an apparent magnitude of F110W=24.3 found in the Par463 pointing of WISP. The J-SNR of the spectrum is 4, and the estimated distance is ~ 800 pc.

In terms of mid-to late T dwarfs, we found 3 objects previously discovered by Masters et al. (2012). WISP0307-7243 is classified as T4 at ~ 500 pc, WISP1232-0033 is classified as T7 at ~ 200 pc and WISP1305-2538 is classified as T9 at ~ 300 pc. Our classifications and distances agree with the previous classification

3D-HST T dwarfs—We find one early T dwarf is COSMOS-23: COSMOS1000+0217 is classified as T3 at ~ 900 pc, with an apparent magnitude of F140W=23.8. The estimated J-SNR of this its G141 spectrum is 5, and the spectrum is a robust fit to the standard. However, given the crowded field, the image is difficult to identify. We found another T dwarf in AEGIS-03, AEGIS1418+5242 is classified as T4, with a high SNR (J-SNR=21) and apparent magnitude of F140W=22.7 implying a distance of ~ 500 pc. The spectrum is a good fit to the spectral standard and there is no visible contamination by nearby objects in the field or other spectral orders. Finally, we detected 2 T dwarfs

in the GOODS fields: GOODSS0332-2741 is classified as T6 with a J-SNR=31 and F140W=22.1 placing it at a distance of \sim 300 pc. GOODSS0332-2749 is classified as a T3 with a J-SNR of 13 at \sim 500 pc. Both spectra are good fits to the spectral standards.

3.6.3. Subdwarfs, Y dwarfs & Binaries

We searched for subdwarfs and Y dwarfs by creating selection criteria for these subtypes. However, we did not find any obvious subdwarfs or binaries in the sample with the two methods. This is unsurprising given that estimates of the ratio of subdwarfs to dwarfs is 1/400 (ref) and the binary fraction of UCDs is very low <10 %.

3.6.4. Borderline L & T dwarfs

There were a few borderline cases that we accepted as UCDs.

3.6.5. Magnitude & Distance Distribution

We create an absolute magnitude-spectral type relation to estimate distances of objects in our observed sample. These relations are built from the relations of [Dupuy & Liu \(2012\)](#). We first computed an offset/color between 2MASS J and H magnitudes and AB Hubble magnitudes by convolving the SpeX standard for a given spectral type with the respective filter. This offset in convolutions is then added to the absolute magnitude-spectral type relations in 2MASS J, H filters to obtain the new relation in Hubble filters. Error propagation is done using Monte-Carlo sampling, we report these relations in Table 3 and show them in Figure 10

We show the distance distribution of the observed sample in Figure (insert fig). While T dwarfs are limited in the nearby \sim 500 pc, M and L dwarfs are observed up to \sim 3kpc; this includes sources outside our effective limiting magnitude. The observed galactic distribution of the UCDs is consistent with the galactic distribution and depths of the pointings in the survey. The farthest L dwarf is at xxx and the farthest T dwarf is xx at xxx pc . This sample include 3 T dwarfs identified by [Masters et al. \(2012\)](#) including perhaps the farthest spectroscopically-identified T dwarf to known. We report the magnitude distribution of our sample in fig xx and table xx. The faintest objects in the sample have magnitudes of F110W=24.3, F140W=25.2, F160W=25.2.

4. PROBING GALACTIC STRUCTURE

4.0.1. *Limiting Magnitudes*

We aim to constrain the number density of UCDs; an accurate estimate of the effective distance/volume of each pointing is crucial. Momcheva et al. 2016 reported the effective depths of all the pointings in 3D-HST, however, given the SNR cut, we expect the a brighter limit than these reported depths. Hence, we adopted the faintness limits of F110W=22.0, F140W=21.5, F160W=21.5 for WISP fields, and F140W=22.5, F160W=22.5 for 3D-HST fields. For the bright end, we used the bright limits of F110W=18.0, F140W=16.0, F160W=16.0 for WISPS fields and F140W=16.0, F160W=16.0 for 3D-HST fields following the peak of the distribution of magnitudes (Figure 12) for all the point sources satisfying the SNR cut. These bright limits correspond to limiting distances hence effective volumes for each spectral type, using the absolute magnitude spectral type relation defined in this work.

4.1. *Monte-Carlo Simulation*

The observed number of UCDs as a function of spectral type depends on the local luminosity function, the probed effective volume, and selection biases. We construct a Monte-Carlo simulation to fully estimate these effects following methods from Reid et al. (1999) and Burgasser (2004). All these steps are illustrated in the graphical model in Figure 13 and explained in this section.

4.1.1. *Local Luminosity Function*

The local luminosity function ($\Phi[mag^{-1}pc^{-3}]$) of UCDs have been measured using various methods. However, this sample of UCD is distant ($\sim kpc$), therefore, to avoid any biases, we simulate a "semi-empirical" luminosity function using two fundamental stellar distributions: the mass function and the age distribution as follows:

- **Mass (M)**, $N_0 \leftarrow \alpha$: we draw a sample of 2×10^5 objects from a power-law mass function parametrized by α for a range of masses between $0.001 M_\odot$ and $0.15 M_\odot$.

$$P(M) = \frac{dN}{dM} \sim \left(\frac{M}{M_\odot} \right)^{-0.6} \quad (9)$$

. We define a normalization factor (N_0) given by

$$N_0 = 0.005 M_{\odot}^{-1} pc^{-3} \sum_{M \in [0.01 M_{\odot}, 0.09 M_{\odot}]} M \cdot P(M) \quad (10)$$

as the number density of objects in this simulated sample with masses between 0.01 and 0.9 in our simulation(Reid et al. 1999, Chabrier 2001). For this part of the simulation, the samples of masses were generated by inverting the cumulative distribution (CDF) and using a random number generator to obtain the corresponding values. The CDF (m) for a given mass m is given by

$$CDF(m) = \frac{1}{C} \int_{M=0.001}^{M=m} P(M) dM = \frac{1}{C} \int_{M=0.001}^{M=m} M^{-0.6} dM \quad (11)$$

, where C is the normalization constant (i.e CDF for $m=0.15$). With this mapping, one can obtain different values of the of m by choosing random number x ($x=CDF$) $\in [0, 1.]$.

- **Age \sim uniform** : we assigned each of these UCDs an age drawn from a uniform uniform age distribution spanning 100 Myr–10 Gyr. Although there are different parametrization of the star-formation history of the Galaxy, this age distribution correlates with the observed scale heights and velocity distribution of the UCD populations (Ryan et al. 2017; Rujopakarn et al. 2010; Aumer & Binney 2009). We then keep the age uniform and vary the scale heights, given that varying the scale height is a simpler parametrization.
- **$T_{eff} \leftarrow SpT \leftarrow (Mass, Age)$** : we assigned a temperature to each of the simulated objects, using a linear interpolation evolutionary model grids from Baraffe et al. (2003). We then converted temperatures to a spectral types (M7-T8) using the polynomial relation from Filippazzo et al. (2015). This resulting distribution of spectral types will then then be used to estimate our selection biases.

4.1.2. *Effective Volumes*

The observed effective volume of each pointing depends on the scale height and the limiting magnitude of the survey. We compute these volumes using the following steps:

- The limiting magnitudes for both 3D-HST and WISPS are defined visually as the peak of the magnitude histogram as shown in Figure 12 and explained in section ???. These magnitudes provide the distance limits for a given spectral type and pointing $d_{max,min}$ determined by

$$\log d_{min,max} = \frac{1}{5}(m - M(SpT)) + 1 \quad (12)$$

where m is the faint or the bright limit of the survey and $M(SpT)$ is the absolute magnitude for that spectral type. For pointings in 3D-HST, we use F140W magnitudes and for WISP pointings we use F110W magnitudes. Absolute magnitude calculations are described in section ???. A complete treatment would account for the effect of dust extinction, however, the pointings in 3D-HST and WISPS are located away from the galactic plane to avoid this problem.

- We adopt a 1-component galactic disk model parametrized by $\theta = (h, l)$ where h and l are the scale height and the scale length of a given stellar population. Using Burgasser (2004), the spatial density of stars in given direction \vec{p} and distance (d) by

$$\rho(\vec{p}, d) = \rho(r, z) = \rho_0 \cdot \text{sech}^2\left(\frac{|z - Z_\odot|}{2h}\right) \cdot \exp\left(-\frac{R - R_\odot}{l}\right) \quad (13)$$

. L is fixed at 2600 pc while h is varied from values of 100 pc, 250 pc, 275 pc, 300 pc, 325 pc, 350 pc and 1000 pc drawn from possible values of scale heights predicted from cooling evolutionary models of UCDS (Ryan et al. 2017). R_\odot and Z_\odot are the sun's position from the galactic center, fixed at 8300 pc and 27 pc respectively. The change from $\rho(\vec{p}, d)$ to $\rho(r, z)$ involves a coordinate transformation from sky to Galactic coordinates.

- $\mathbf{V}_c \leftarrow \theta=(h, l)$ and $\mathbf{V}_{eff} \leftarrow (\mathbf{d}_{max}, \mathbf{d}_{min}, \mathbf{V}_c)$: given the Galactic structure model, we compute a volume correction (V_c) up to distance d , in a given direction \vec{p} . This term is the ratio of exponential density to a uniform space density in a given direction.

$$V_c = \frac{\int_0^d \rho(x, \vec{p}) \cdot x^2 dx}{\int_0^x x^2 dx} \quad (14)$$

, where x is the 3D-distance in that line of sight. The effective volume of each pointing (\vec{p}) and spectral type is

$$V_{eff}(\vec{p}) = V_c(d_{max} - d_{min}, \vec{p}) \cdot (d_{max}^3 - d_{min}^3) \cdot \Delta\Omega \cdot \frac{1}{3} \quad (15)$$

. Where the $\Delta\Omega$ is the solid angle of each pointing fixed at $\Delta\Omega \approx 3.47 \times 10^{-7}$ radian² for each pointing.

4.1.3. Selection Effects

Because we applied several selection criteria to narrow down our sample for visual confirmation, it is possible we may have missed a few UCDs in the WISPS/3D-HST fields; particularly low SNR or peculiar objects due, in part, to uncertainties in spectral indices. Hence, the observed volumes objects must be corrected by a factor proportional to our selection biases. To fully quantify these effects, we generated a distribution of low-resolution spectra uniformly sampling our SNR distribution across a wide range of SNRs and measured their recovery rate through this selection process by augmenting the SpeX sample to cover 3 orders of magnitude in SNR. To create this sample, we picked the top 20 highest SNR spectra with a median SNR between 50 and 200 L0-T9 objects in the SpeX sample, we added Gaussian noise each spectrum for an iteration of 10^3 steps creating a new sample of 21800 spectra. Each new "degraded" spectrum is created as

$$\{F(\lambda_i)\} \sim \text{Normal}(< F(\lambda_i) >, \sigma^t(\lambda_i)) \quad (16)$$

. $\sigma^t(\lambda_i)$ is the target noise at a wavelength λ_i , and $< F(\lambda_i) >$ is the flux of the original spectrum at that wavelength. We computed all relevant statistics for each of the degraded spectra, including J-SNR, spectral indices, F-test, and the two χ^2 s. We applied our selection processes to this sample of simulated spectra by measuring spectral indices and applying first F-test criterion where F-test < 0.4 , box index-index selection criteria and the random forest classifier.

In addition, after degrading the spectrum, the object will change its original classification. We defined a selection probability that accounts for the number of objects falling outside our classification range (M7-Y0) after degradation and the selection process itself in a given signal-to-noise range (Δ J-SNR bin of 2.0). We denote this probability of selection of $\mathcal{S}(\text{J-SNR}, \text{SpT})$

$$\mathcal{S}(\text{J-SNR}_i, \text{SpT}) = \frac{N_{s,i} + N_{m,i}}{N_{tot,i}} \quad (17)$$

where N_s is the number selected spectral type and SNR bin, and N_{tot} is the total number of objects in that bin. Where $N_{s,i}$ is the number of objects in a bin i, selected by our selection process and

$N_{m,i}$ is the number of objects in a bin i that fall outside the spectral type range of M7-Y2 after degradation. $N_{tot,i}$ is the total number of spectra in that signal-to-noise ratio bin. These selection probabilities are showcased in Figure x.

For each simulated spectral type from the mass function (section 4.1.1), we computed a selection probability \mathcal{S} parametrized by the expected signal-to-noise ratio (J-SNR) and spectral type (SpT) using the following steps:

- $\mathbf{d} \leftarrow (\theta=(\mathbf{h}, \mathbf{l}), \mathbf{d}_{max}, \mathbf{d}_{min})$: we assign a distance to each of drawn from the Galactic structure model. The likelihood of distance (d) given a spectral type (SpT) pointing \vec{p}

$$P(d|\vec{p}) \sim \rho(d, \vec{p}) \cdot d^2 \quad (18)$$

. We then assign each object a randomly drawn distance from all the 533 pointings/directions in both surveys. For a given spectral type the distance is limited to $d_{min}/2 < d < 10 \times d_{max}$ to account for objects scattered in the observed volume. Samples for this part of the simulation were generated using Pymc for a number of samples $N=20000$, sampling each scale height independently using a standard Metropolis-Hastings Algorithm.

- **J-SNR** $\leftarrow (\mathbf{F110W}, \mathbf{F140W}, \mathbf{F160W}) \leftarrow (\mathbf{d}, \mathbf{SpT})$: we estimate an observable signal-to-noise ratio of each object as observed by the WFC3 instrument based on the observed sample. We fit a second-degree polynomial to the observed magnitudes (F110W, F140W, F160W) and SNR-J of our observed sample. We then use our derived absolute-magnitude spectral type relations to estimate the apparent magnitude of each object in our simulated sample based on its randomly-assigned distance and spectral type. The apparent magnitude- J-SNR relation is then used to estimate a signal-to-noise ratio as observed with the WFC3 instrument.
- $\mathcal{S} \leftarrow (\mathbf{J-SNR}, \mathbf{SpT})$: we assigned a selection probability, as previously defined, to every simulated object in the observed, that is an object with magnitude and signal-noise ratios within our cuts (J-SNR < 3 and F110W > 22.5 (the limiting magnitude from 3D-HST)).

The expected number of expected objects per spectral type is then by a simple product of selection probabilities, effective volume scaled by the normalization factor.

$$N_{sim}(\text{SpT}) = N_0 \cdot V_{eff}(\text{SpT}) \cdot \sum_i \mathcal{S}(\text{J-SNR}_i, \text{SpT}) \quad (19)$$

. We compared these numbers to the observed numbers of UCDs for each age distribution in figure 17

4.2. Results

The resulting spectral type distribution is consistent with expectations given atmospheric cooling effects (Burgasser 2004) from evolutionary models. As UCDs age, they quickly pile up on at the lower end of the spectral type distribution and cooler temperatures. The effective volume for each spectral type and scale heights span 6 orders of magnitude in pc^3 , and given that earlier spectral types probe larger volumes, the effect of scale heights is more distinguishable for these types ($\text{SpT} \leq T5$). The resulting distribution of distances is smooth, given the simplicity of our Galactic structure model. Ryan et al. (2017) estimated a change in scale height of ($\Delta h \sim 50$ pc) in the mid-L dwarf regime by comparing galactic models for different cooling scenarios; while the scale height in for late M dwarf and L is consistent with our simulations, and despite the high accuracy in spectral types for the sample of UCDs presented in this study, the relatively small sample size of L& T dwarfs might not put meaningful constraints on the scale height variations. Nevertheless, the total number of observed M7-T8 dwarfs (136 ± 11) is consistent with a scale height between 325-350 pc.

We predict more T dwarfs observed, in part due to a possible underestimation of the observed volume given that limiting magnitudes were visually estimated [there has be a more empirical way of doing this, like KDEs]. Moreover, the L/T transition region is sensitive to unresolved binaries (Bardalez Gagliuffi et al. 2014). Burgasser (2007) shows that given a spectral binary fraction of $\sim 10\%$, the surface densities for volume-limited sample of primaries and combined systems are similar but present a slight bump ($\Delta\Sigma \lesssim 5 \times 10^{-5} \text{ deg}^{-2}$) for early T dwarfs. Given our total search area of $\sim 0.6 \text{ deg}^2$, we do not expect a significant effect of the spectral binary fraction to the reported densities, hence we assumed that none of the UCDs in this study are unresolved binaries in our simulation.

Metallicity effects affect the number of subdwarfs we expected in this sample. UCDs in the thick disk and the halo have similar kinematic ages with stellar populations in these parts of the Galaxy; and UCDs at different metallicities follow different evolutionary tracks. L subdwarfs in the local neighborhood are therefore rare, and this study does not significantly probe large volumes in the thick disk and halo. [Lodieu et al. \(2017\)](#) found $0.04 \times \text{deg}^{-2}$ L subdwarfs in the UKIDSS/SDSS fields; in fact, we expect the number of subdwarfs to be ~ 400 times lower than the expected number of dwarfs in the sample. Although the parallel fields in 3D-HST & WISP are deep, the total search area remains low, hence it is not surprising that we did not find any L subdwarfs in the sample.

5. SUMMARY

The WISPS & 3D-HST surveys provide NIR G141 (1.1-1.14 μm) spectroscopic data and broadband F140W, F110W & F160W photometry for thousands of galaxies and point-sources observed in parallel mode with other on-going HST surveys. We made a point-source cut using in the surveys and obtained 271915 point-sources. Using NIR spectral indices that sample the prominent H₂O and CH₄ absorption features in UCD atmospheres, we created selection criteria based on a calibration sample of templates. We have presented two methods for selecting UCDs in deep HST surveys potentially applicable future infrared parallel surveys. Both methods rely on spectral indices defined to trace H₂O and CH₄ features prominent in the NIR band of UCDS. The box selection method is efficient (completeness $>90\%$) but with relatively high contamination rates that could be significantly reduced by eliminating the lowest SNR sources. This method is not effective for selecting very low SNR sources due to large scatter in indices and early M-dwarfs as the absorption features in these wavelength ranges are shallow. However, these spectral indices are designed to selected T-dwarfs with high accuracy (completeness $>90\%$, contamination $<1\%$). The overall contamination/false positive rate for this method for spectral types of L0–L5 is $\sim 87\%$. A second method uses a random forest classifier to distinguish UCDs from other extragalactic contaminants or artifacts with an accuracy score of 99.5% in cross-validation. The false positive rate of this method for spectral types of L0–L5 is $\sim 62\%$. Both methods rely on a training set of known UCD samples and can be combined. With

these two methods, we have used these data to obtain 166 spectra of M7-T9 UCDs up to distances ~ 4 kpc.

We estimated the expected number of UCDs given a galactic structure model with scale height (h) as a free-parameter. Using a point-source limiting magnitude, we measured the effective volumes of the survey for various values of the scale height. To address intrinsic biases in our selection method, we use a Monte-Carlo simulation to reproduce a distribution of spectral type based on a set of fundamental distribution: mass function, age distribution and conversion/polynomial relation from UCD evolutionary models and our sample. We use the galactic structure model to draw a distribution of distances. With these distributions, we create a selection probability function based on sample of "degraded" templates. The final steps involve summing over selection probabilities. The predicted number of UCDs is consistent with a scale height of $325 \text{ pc} \leq h \leq 350 \text{ pc}$.

Future space missions such as JSWT, Euclid will be contaminated by UCDs. [Ryan Jr. & Reid \(2016\)](#) predicted that the number density of UCDs (M8-T8) in JSWT fields peaks around $J \sim 24$ mag with a total surface density of $\Sigma \sim 0.3 \text{ arcmin}^{-2}$. With the *Large-Scale Synoptic Telescope* (LSST), and the *Wide-Field Infrared Survey Telescope* (WFIRST), we expect an increase in both sample size and spectral type accuracy, expanding the parameter space necessary to put significant constraint on the star formation history of the Milky Way in general and the mass function of UCDs in particular ([LSST Science Collaboration et al. 2009](#), [Spergel et al. 2015](#)).

ACKNOWLEDGMENTS

This work is based on observations taken by the 3D-HST treasury program (GO 12177 and 12328) with the NASA/ESA HST, which is operated by the Association of universities for Research in Astronomy, Inc. under NASA contract NAS5-26555.

CA thanks the LSSTC Data Science Fellowship Program, which is funded by LSSTC, NSF Cyber-training Grant #1829740, the Brinson Foundation, and the Moore Foundation; his participation in the program has benefited this work.

Software: Astropy(Collaboration et al. 2013), Matplotlib (Hunter 2007), SPLAT(Burgasser 2014b), Scipy(Virtanen et al. 2019), Pandas, Seaborn (Waskom et al. 2014), Daft, Pymc3(Salvatier et al. 2016)

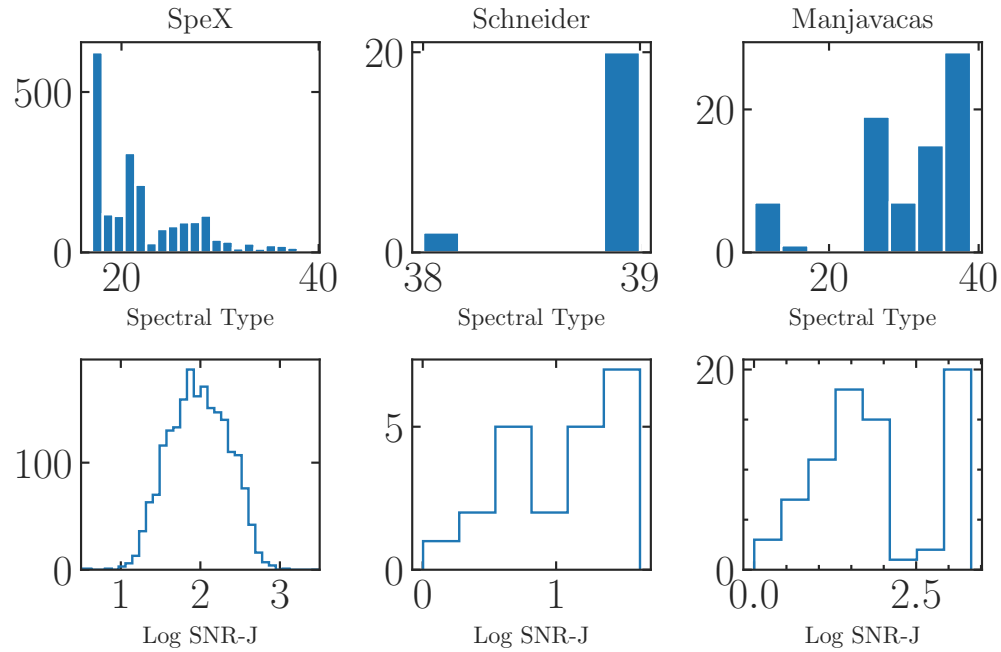


Figure 1. Distribution in spectral type and signal to noise of three calibration samples of UCDs used in this study

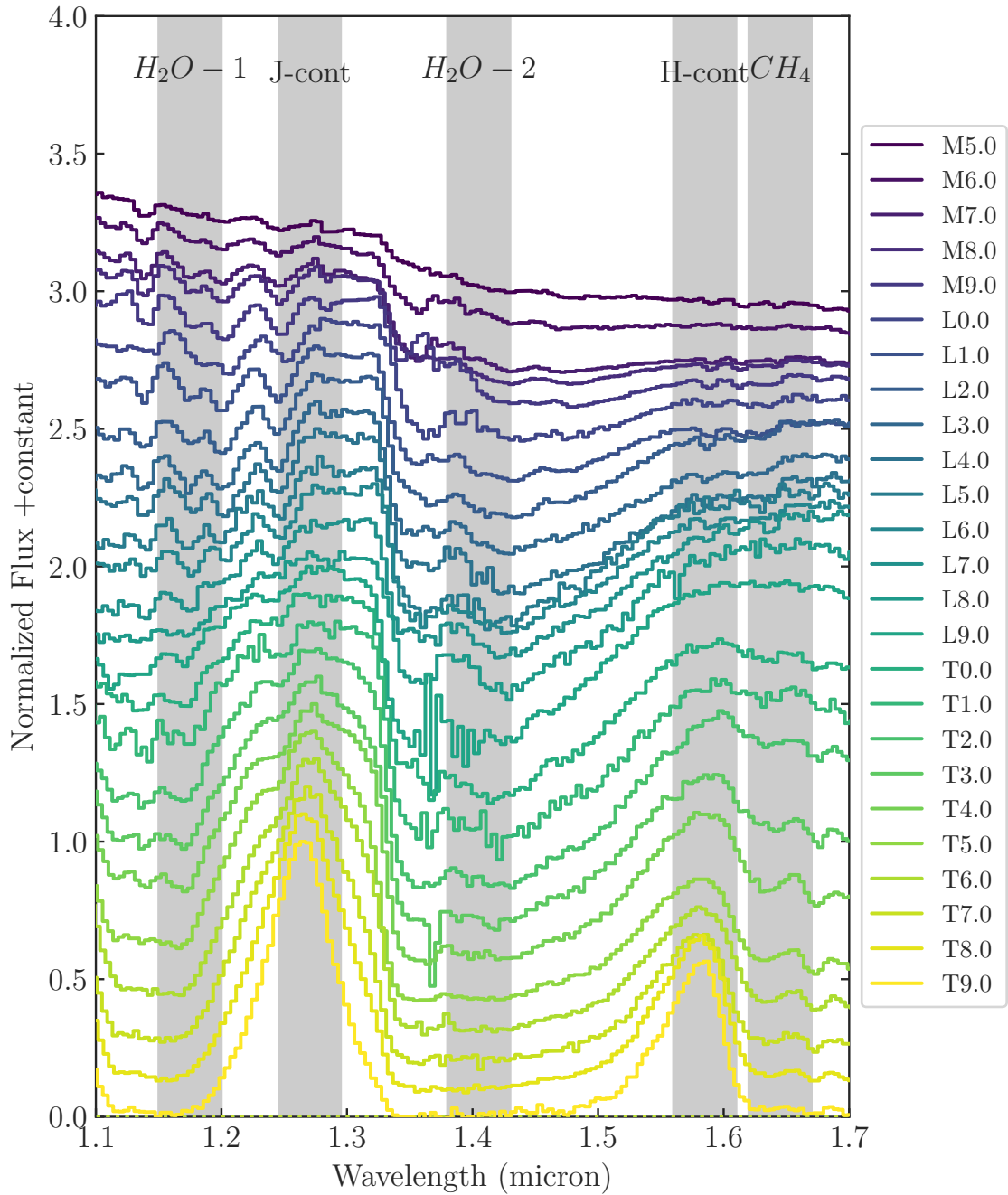


Figure 2. M5-T9 low resolution SpeX spectral standards (Kirkpatrick et al. 2010) with highlighted bands showing the definition of spectral indices used in this study

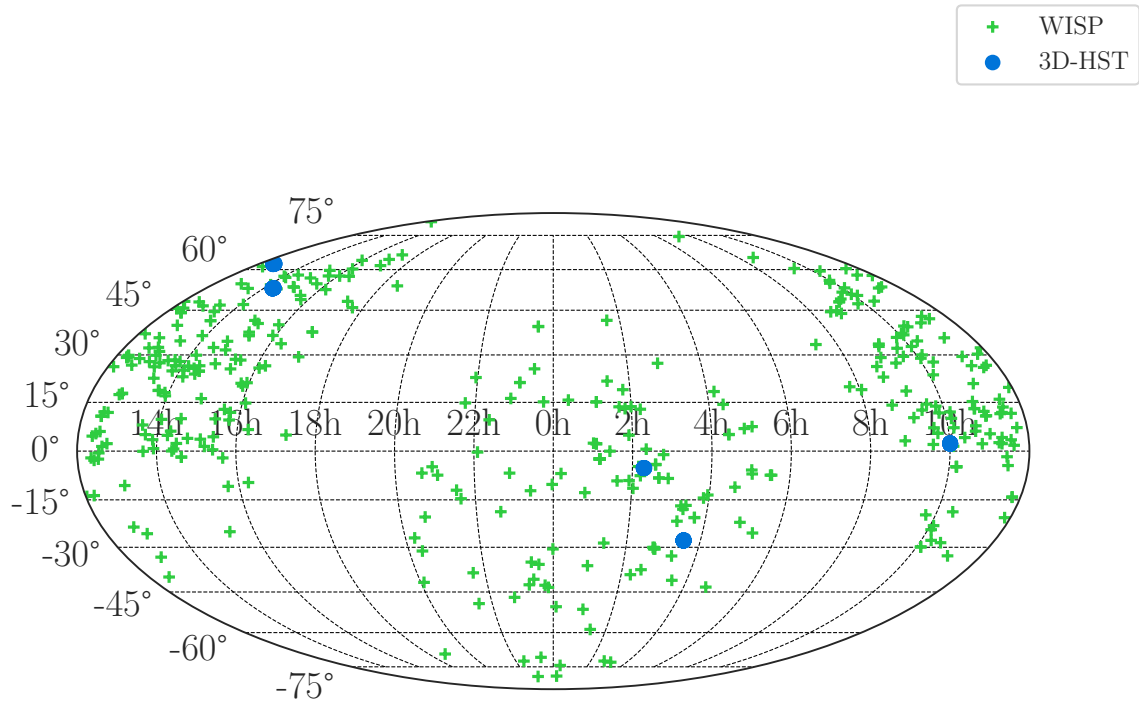


Figure 3. Sky distribution all the pointings in WISPS and 3D-HST used in this study

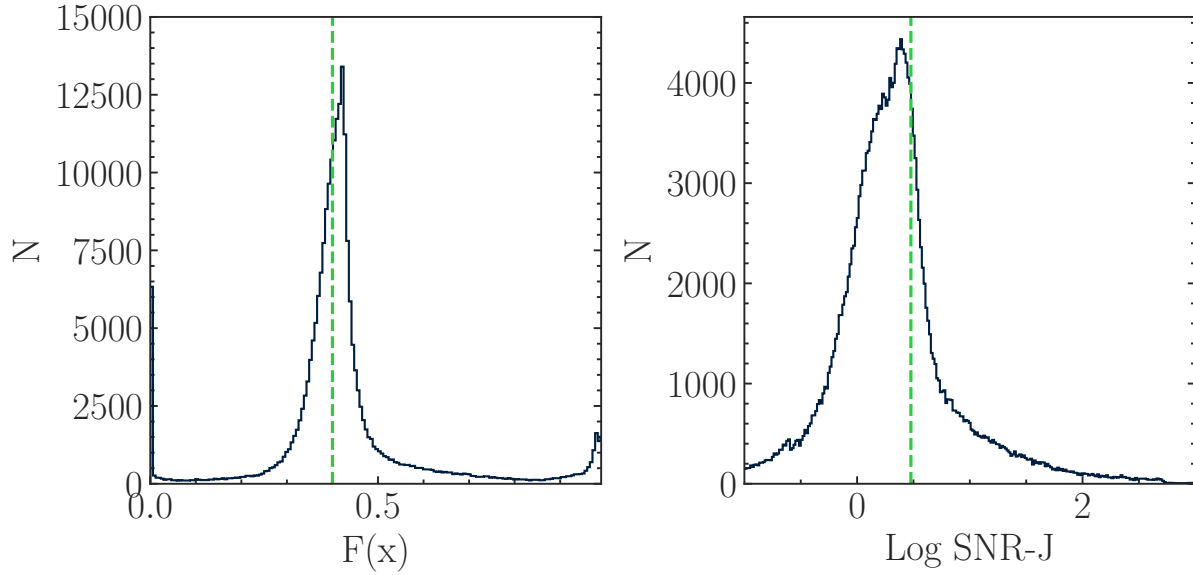


Figure 4. F-test and SNR-J distributions of all Spectra in both surveys showing the cuts at 0.4 and 3 respectively

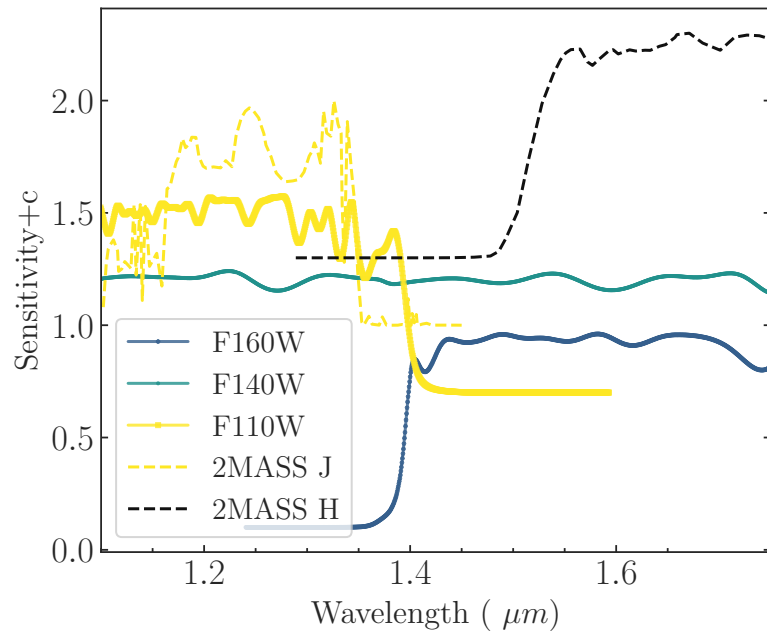


Figure 5. Comparison between spectral coverage of different WFC3 and 2MASS filters used in this study. We used these filters to estimate absolute magnitudes of our UCD sample

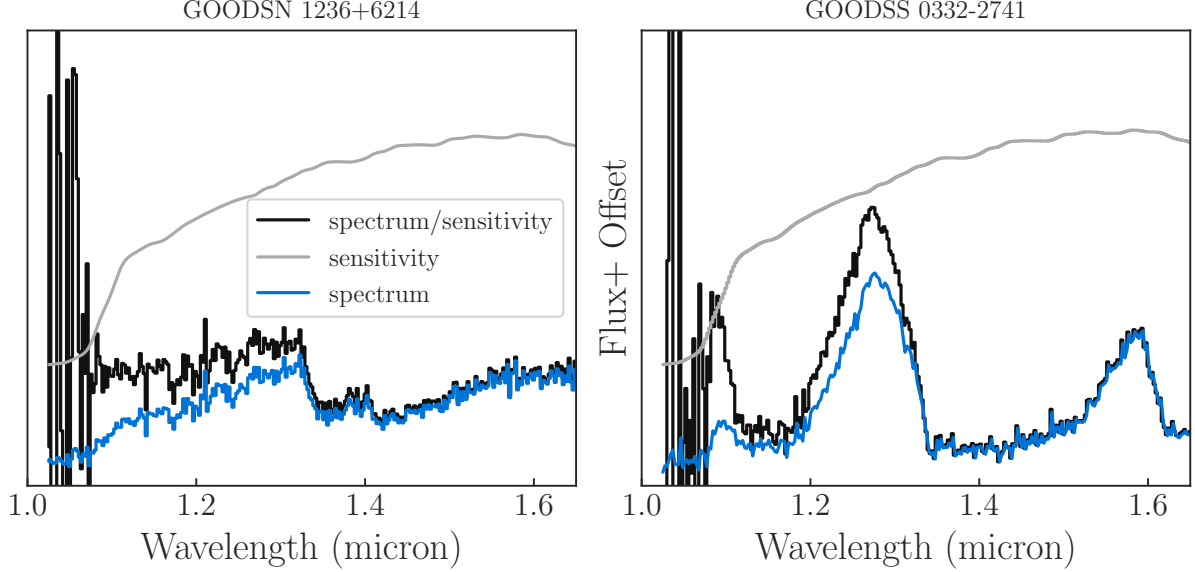


Figure 6. Example of 2 HST-3D spectra before and after continuum correction to obtain the correct slope. The sensitivity curve is plotted in grey.

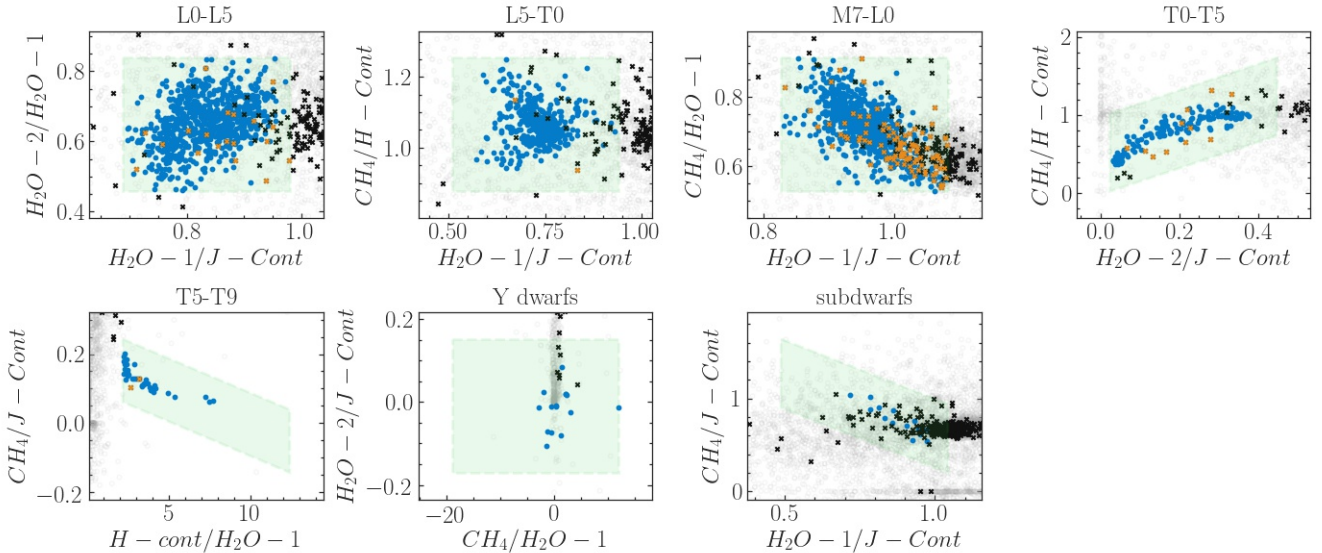


Figure 7. Best selection criteria for different subtype ranges. The grey points are the contaminants after we applied both a J-SNR cut and and F-test cut, the blue points are the set of templates (from the calibration samples) used to define these boxes. The crossed black points are the real UCDs confirmed after visual inspection and the orange crosses are the UCDs that have spectral types for each particular box (e.g a L2 UCD would be colored orange in the L0-L5 while an L7 would be colored black the L0-L5 box)

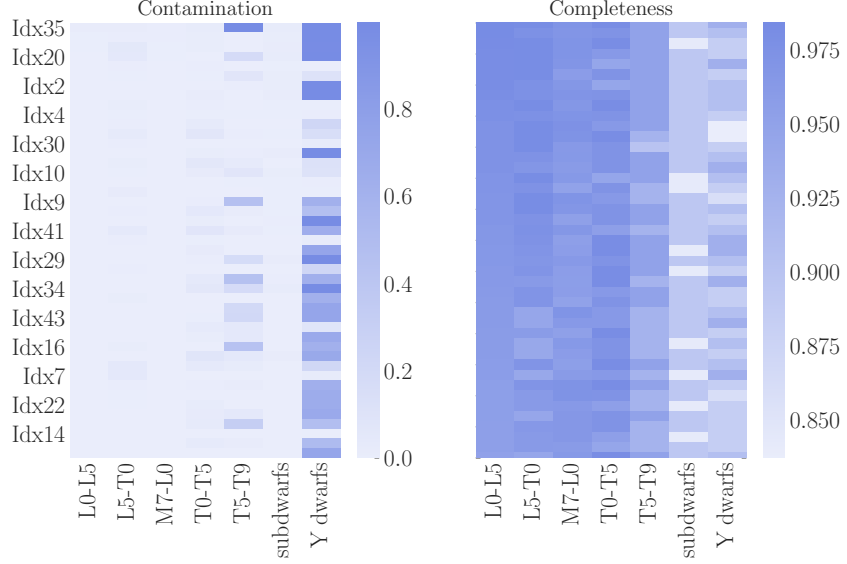


Figure 8. Visual Representation of CPT and COMP statistics for all possible combination of spectral indices for each subtype range. Although the overall completenesses of each box is high ($>80\%$), the contamination may vary. We only use selection criteria with the lowest possible contamination, however, any combination of these indices could be useful for selecting UCDS in other surveys

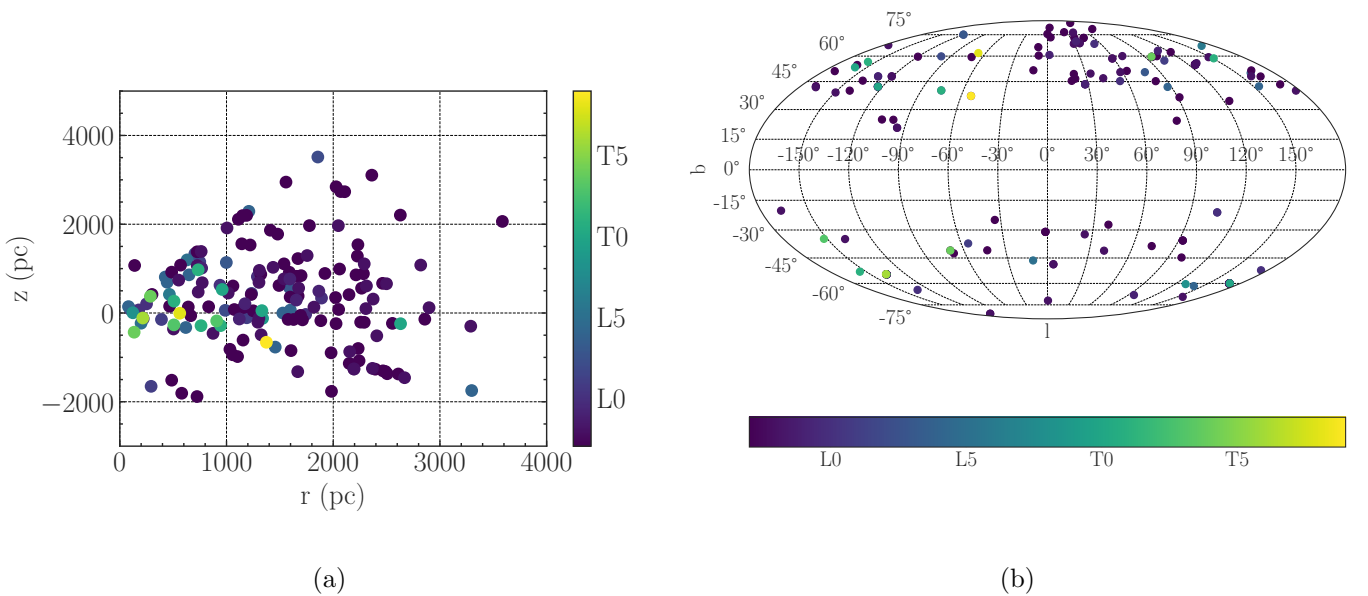


Figure 9. (a) Distance distribution of the UCD sample (b) Galactic distribution of the UCD sample

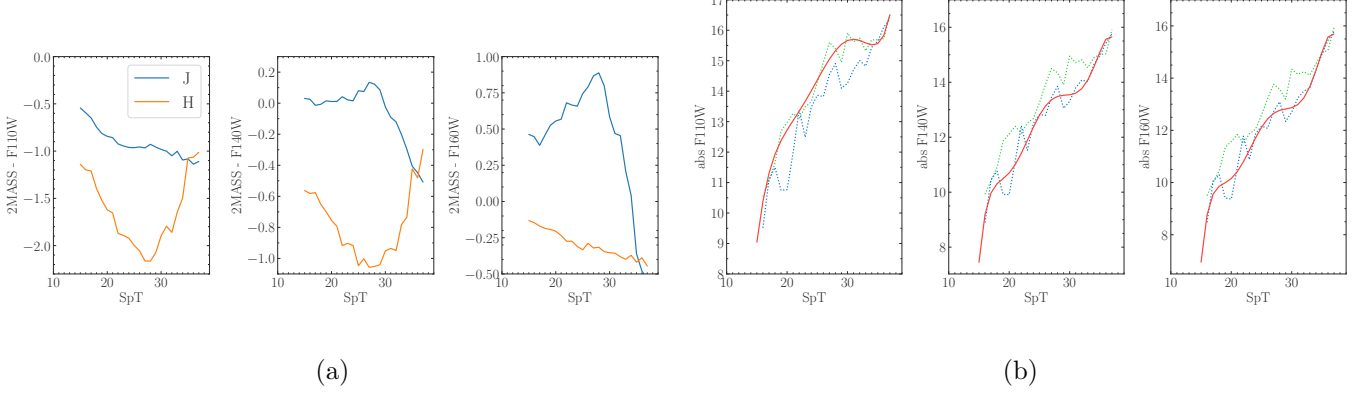


Figure 10. (a) Offsets between 2MASS J, H magnitudes and HST F110W, F140W, F160W magnitudes as a function of spectral type (b) Absolute magnitude-spectral type relations for HST and 2 MASS filters. For HST filters, the dotted green curve shows the derived relation using only the offset between the respective HST filter and 2MASS J filter while the blue curve shows the derived relation using the offset with the 2MASS H filter. The solid line shows a best-fit 6th-order polynomial used, considering the wavelength coverage of the respective filters (figure 5). We report the coefficients of these polynomials in table 3

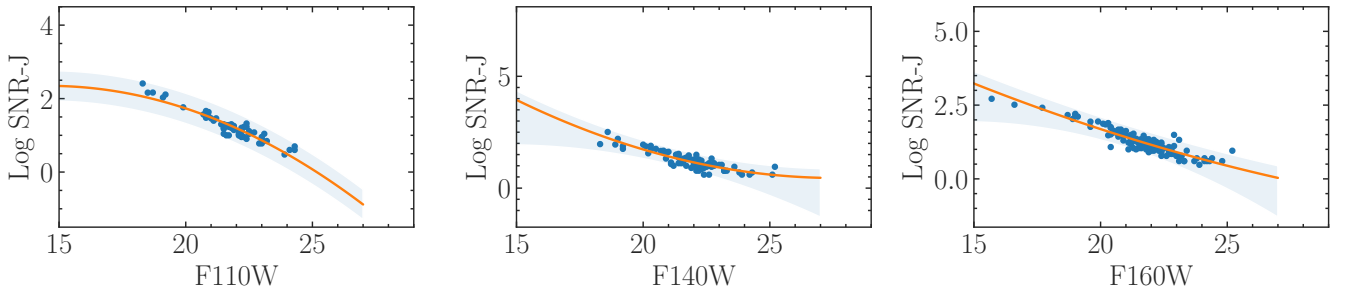


Figure 11. Linear fits between SNR-J and apparent F110W, F140W, F160W magnitudes using the sample of UCDs. These relations are reported in table 3 and used to estimate SNR-J for different apparent magnitudes

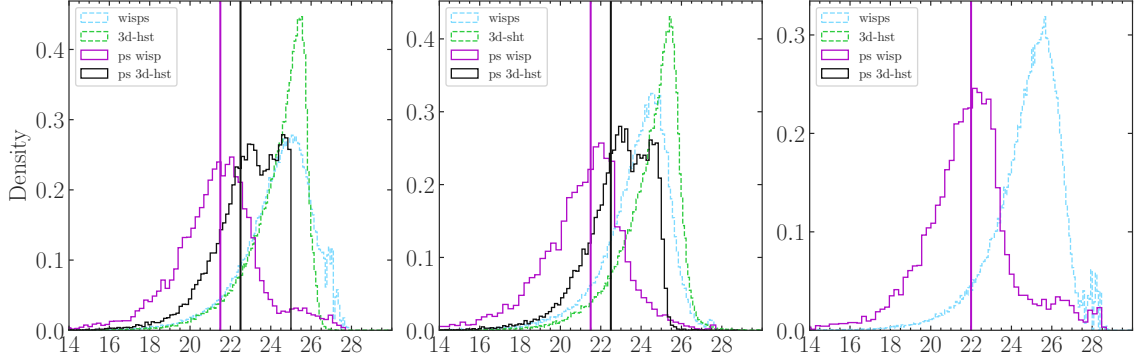


Figure 12. Magnitude distribution of point sources (solid lines) and all the sources (dotted lines) in both WISP & 3D-HST. We estimate the limiting magnitudes based on the distribution of point sources. For wisps the limiting magnitudes are F110W=22.0, F140W= 21.5, and F160W= 21.5. For 3D-HST the limiting magnitudes are F140W=22.5 and F160W. These magnitudes are used to compute the effective volumes for each spectral type

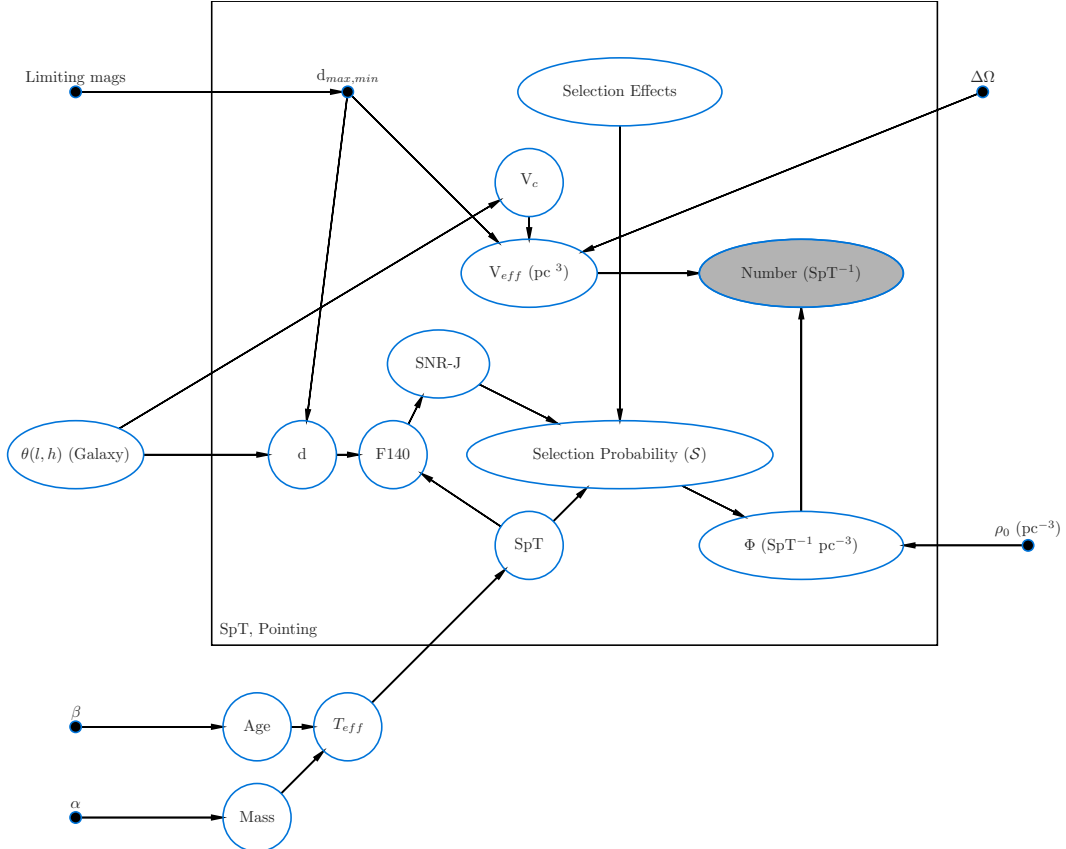


Figure 13. Graphical Model showing the simulation process

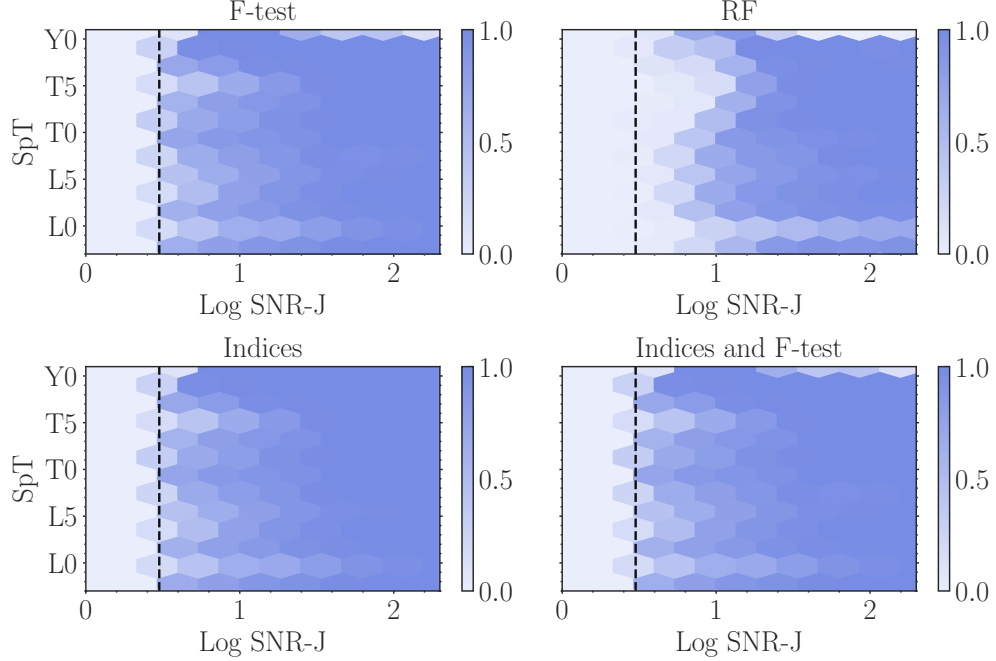


Figure 14. Visualization of our selection function as a function across spectral type and SNR-J. The label "F-test" indicates spectra with $F\text{-test} < 0.4$, the label "RF" indicates the spectra labelled as UCDs by the random forest classifier, and the label "Indices" indicates the spectra selected by our best selection criteria. The bar indicates the selection probability defined as the number of spectra selected over the total number of spectra in each SNR-J, spectral type bin. In the Monte-Carlo simulation, we use the most-selective selection function.

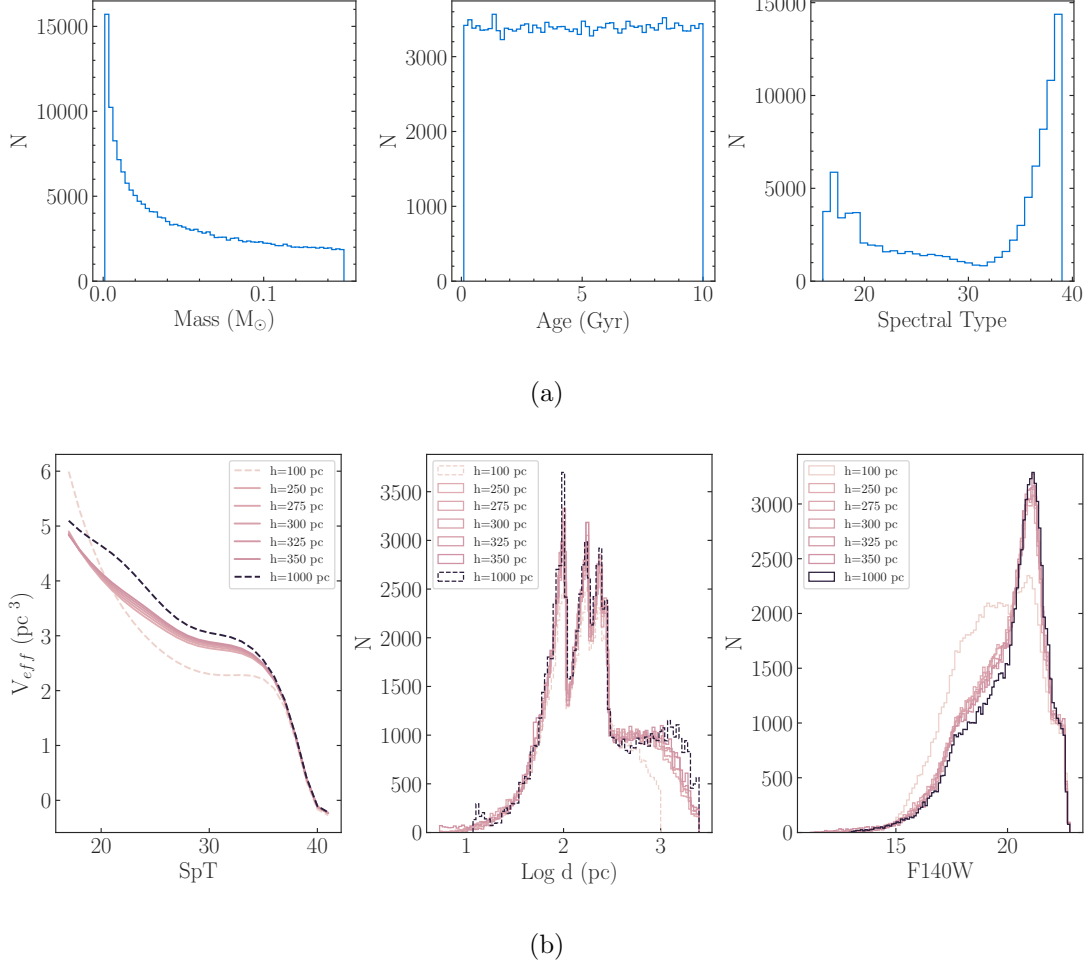


Figure 15. (a) Monte-Carlo simulation: distribution of randomly drawn masses, a uniform age distribution and spectral types (b) distribution J-SNRs, distances apparent F140W following relations defined in this work assuming different scale heights. We also show the computed volume for each spectral type

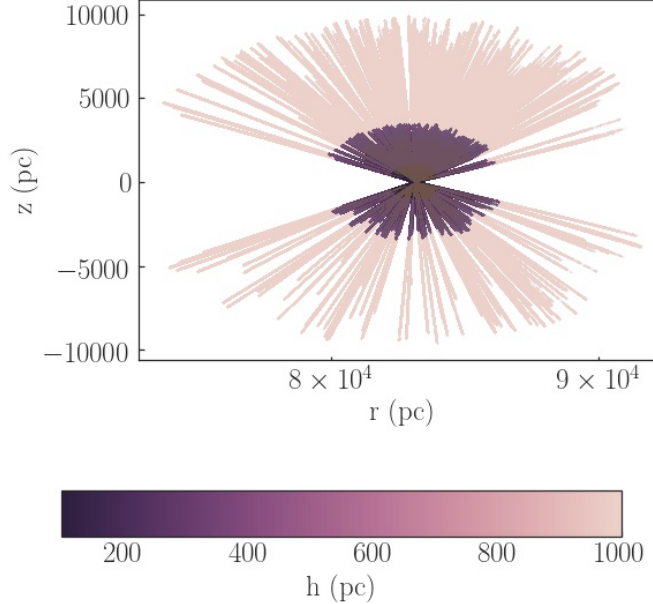


Figure 16. Monte-Carlo simulation: distribution of galacto-centric r, z sampled from the likelihood function $P(d)$ for all 533 pointings up to a distance of $5h$

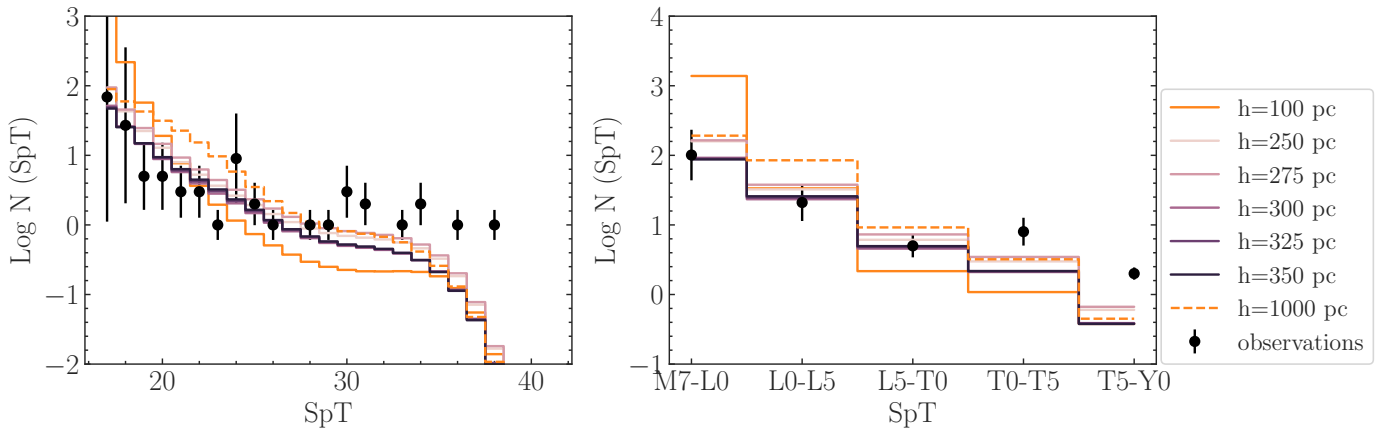


Figure 17. Comparison between the measured number densities and the expected number densities based on the Monte-Carlo simulation based on different age distributions. These estimates are based on limiting magnitude F140W <21.5 and SNR-J >10 which eliminates most of our T dwarf sample

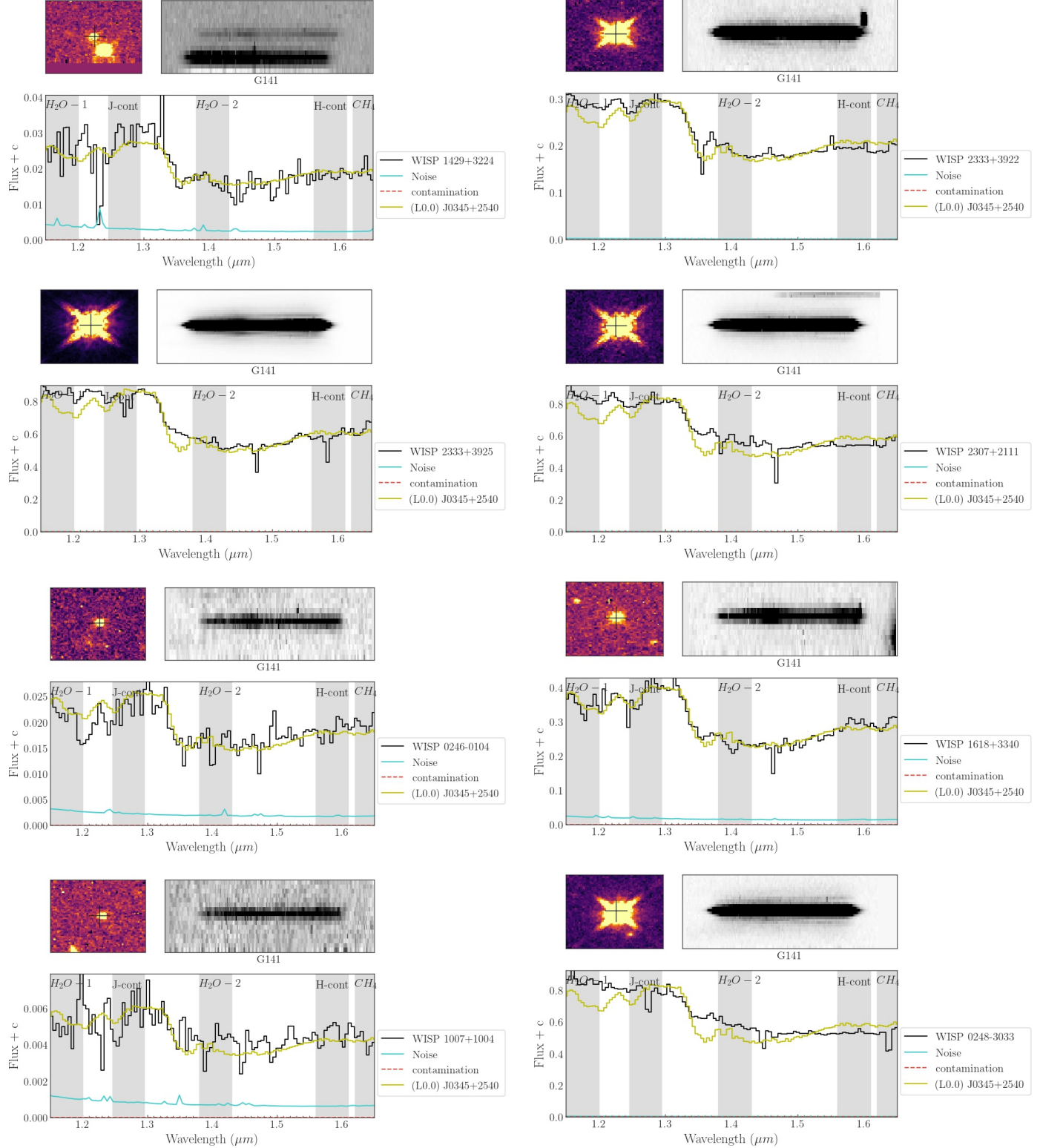
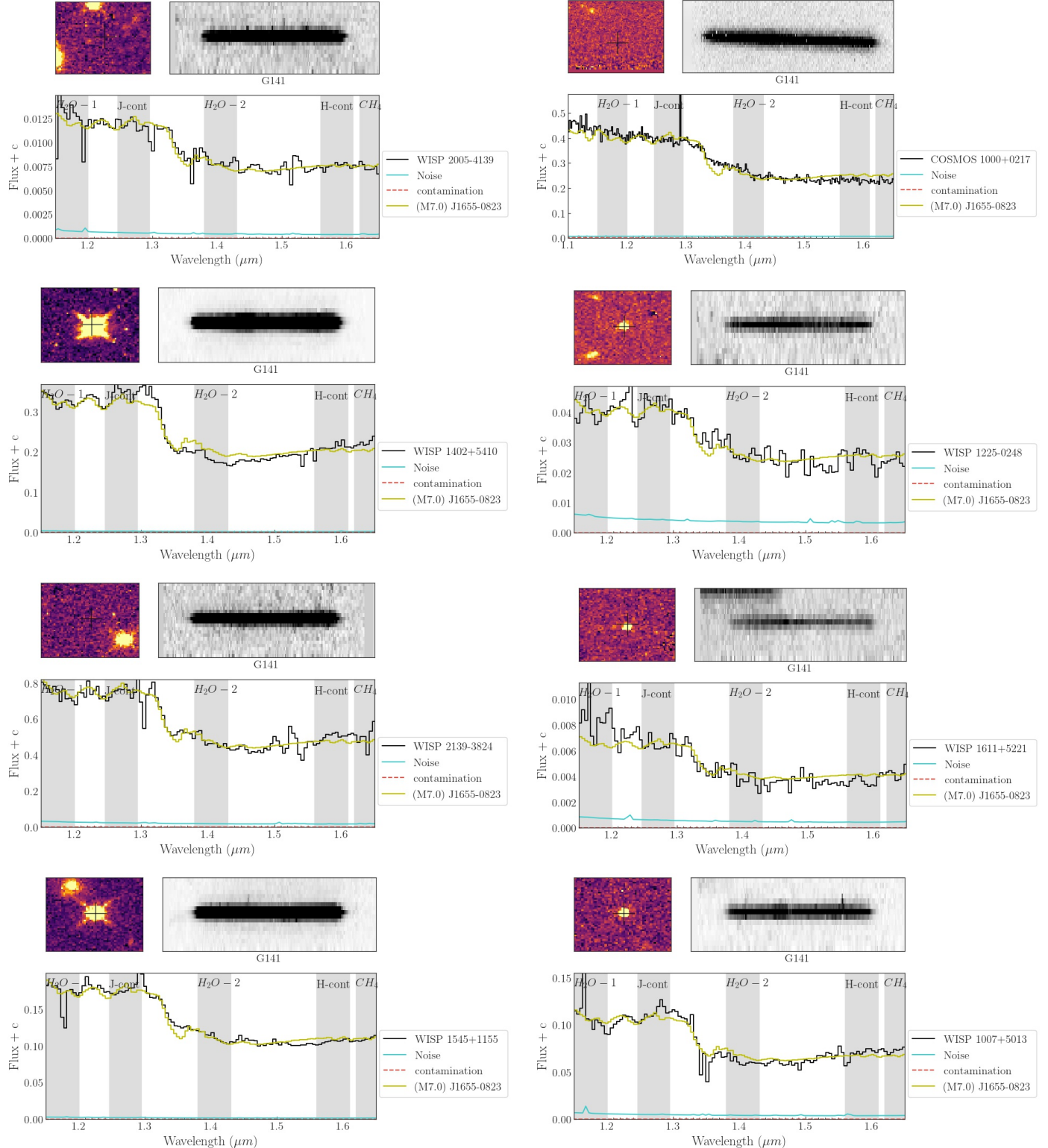
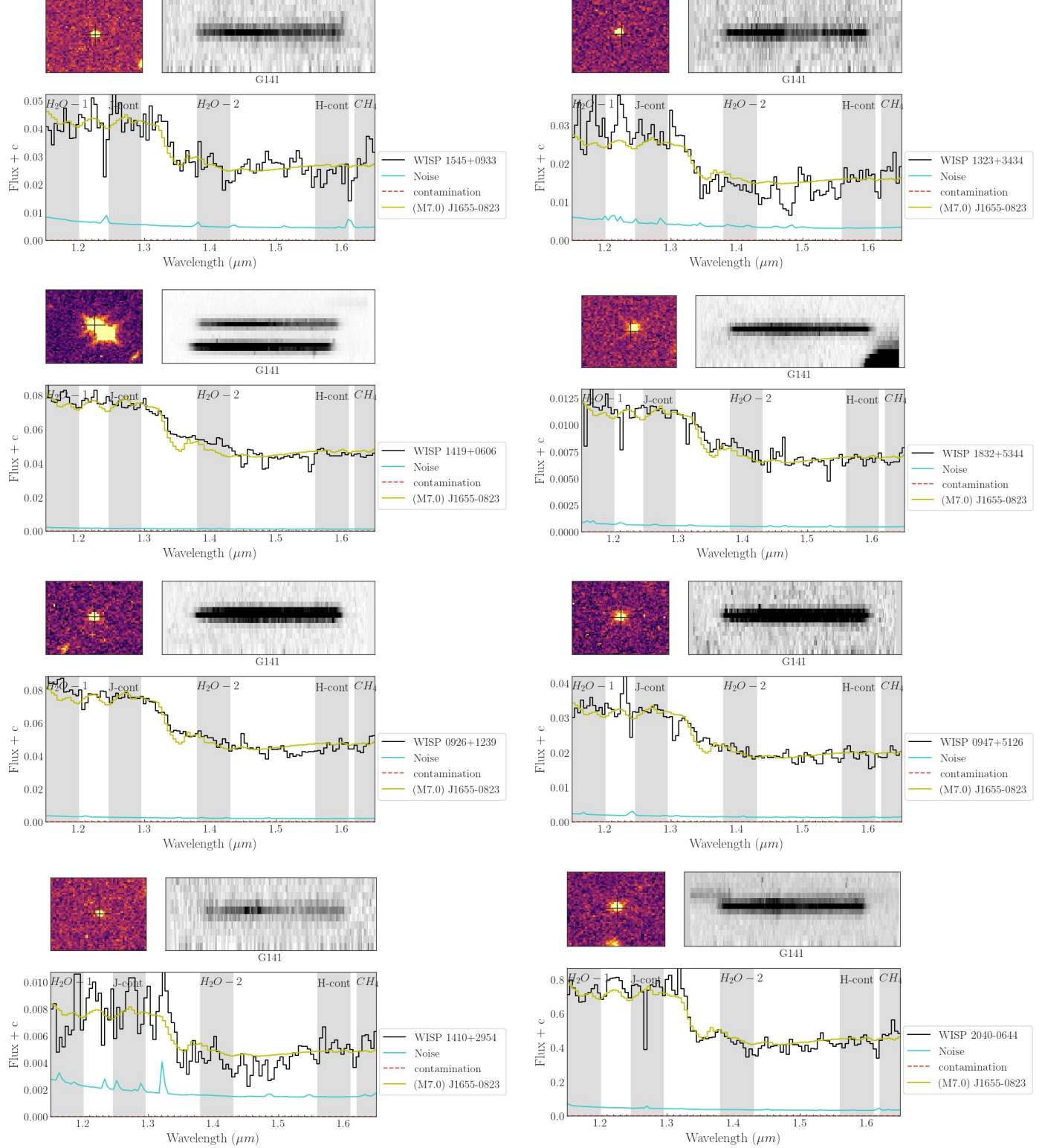
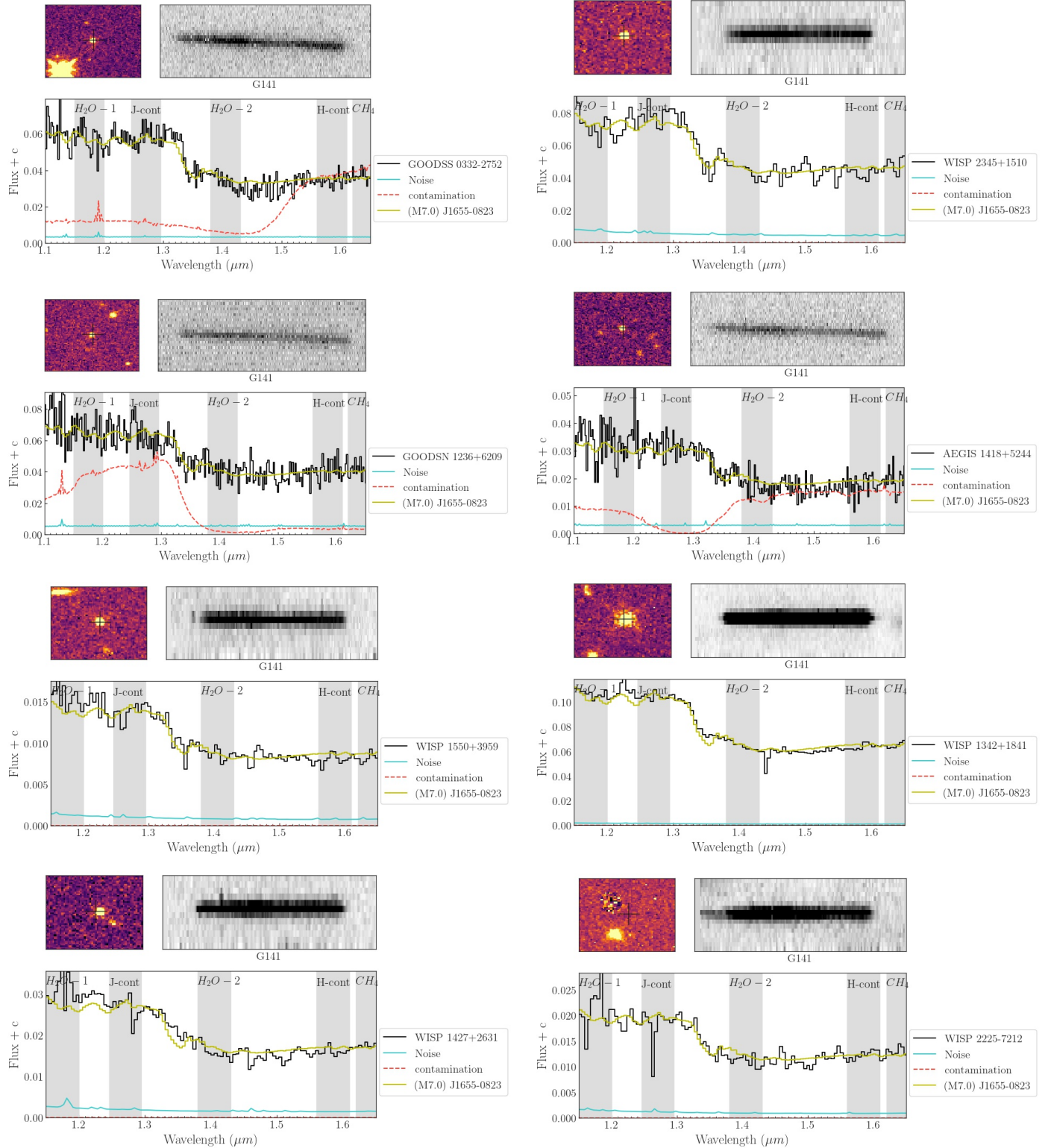


Figure 18. Spectra of UCDS in both surveys. The bottom plot shows the 1D spectrum fit to a spectral standard. The noise and the contamination are also shown, the top left plot shows the WFC3 image acquired in either F140W, F160W or F110W filter and the top-right plot shows the cutoff of the G141 spectrum for that extracted object.

**Figure 19.** cont.

**Figure 20.** cont.

**Figure 21.** cont.

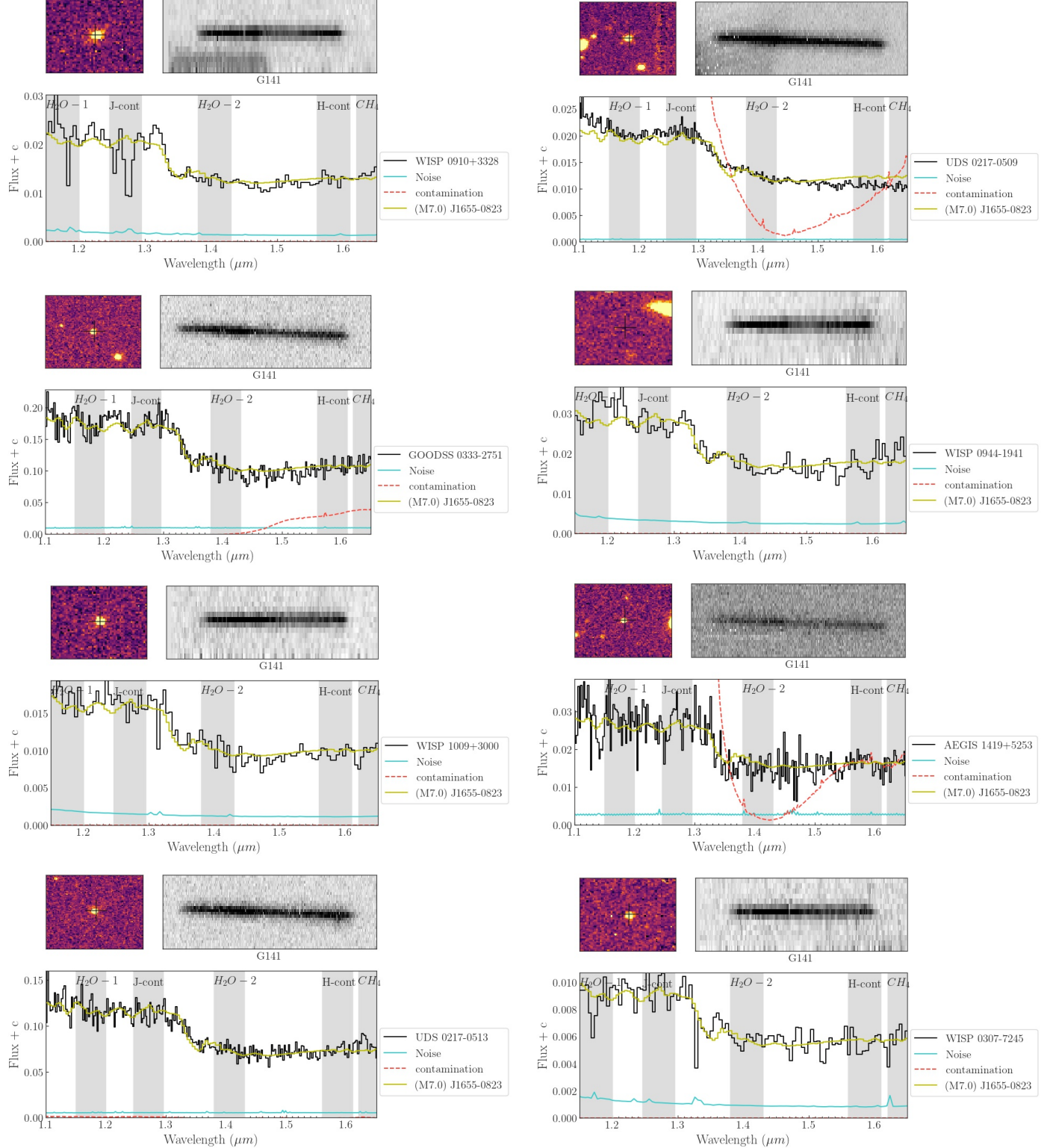
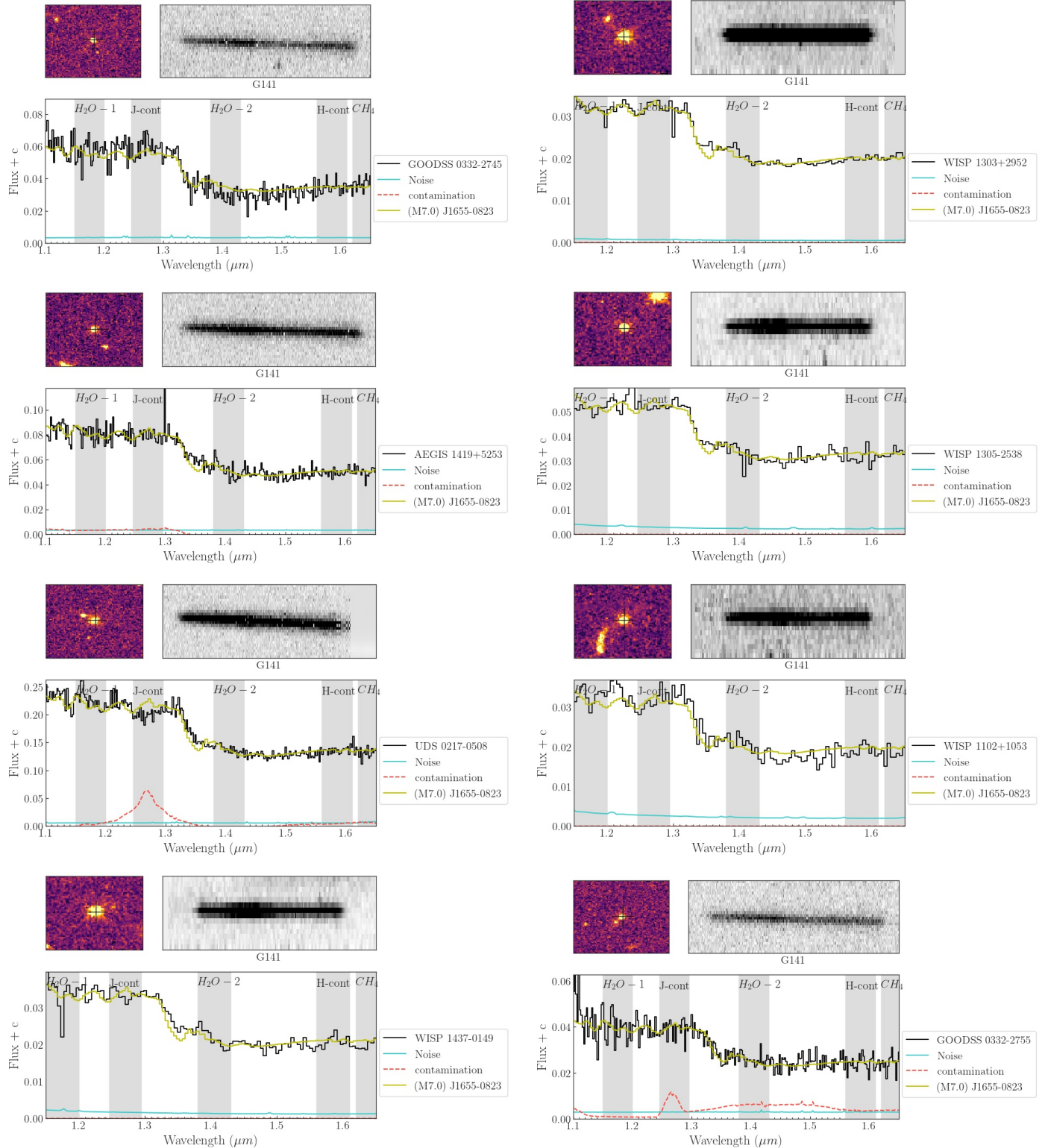
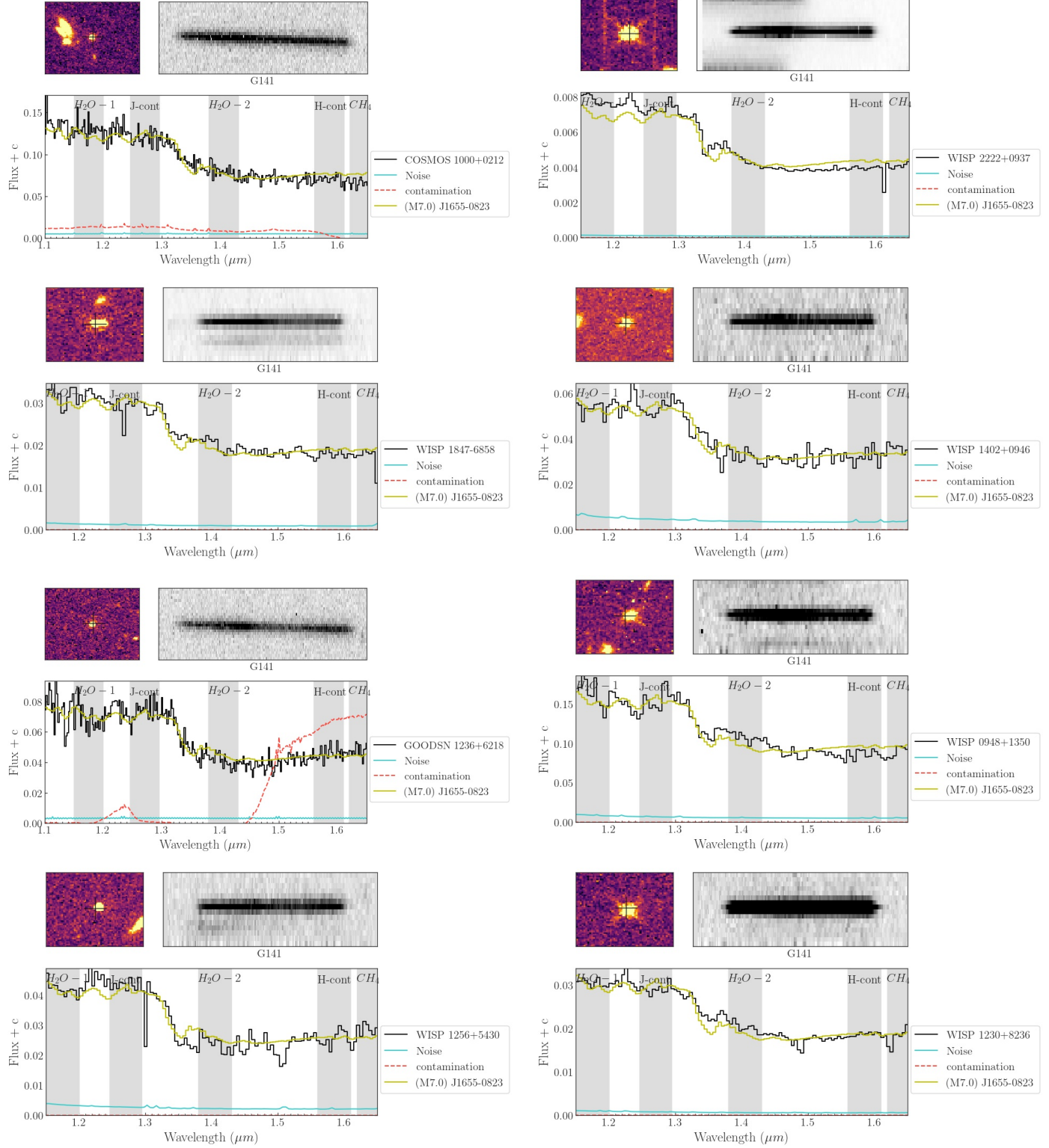
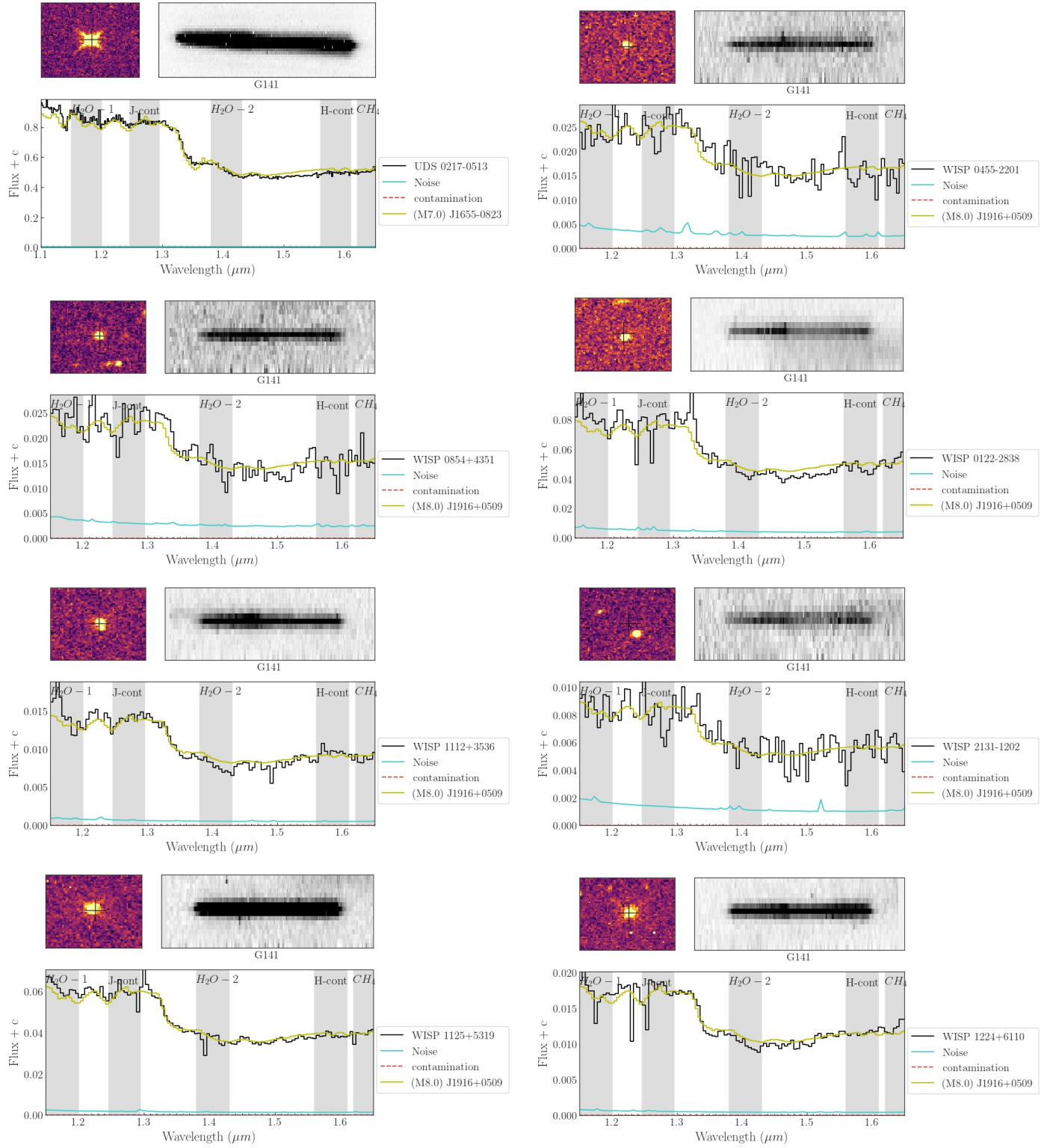
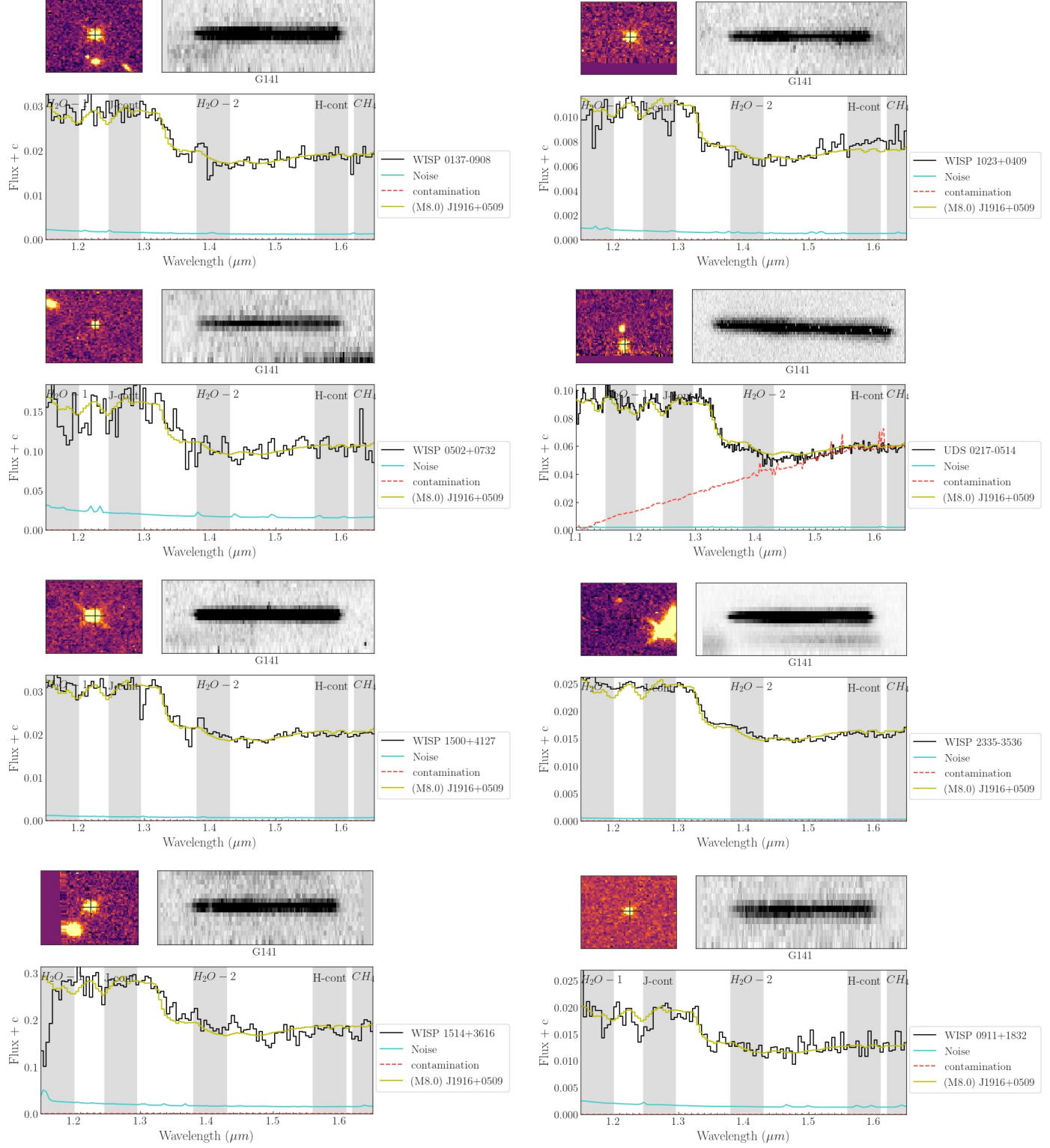


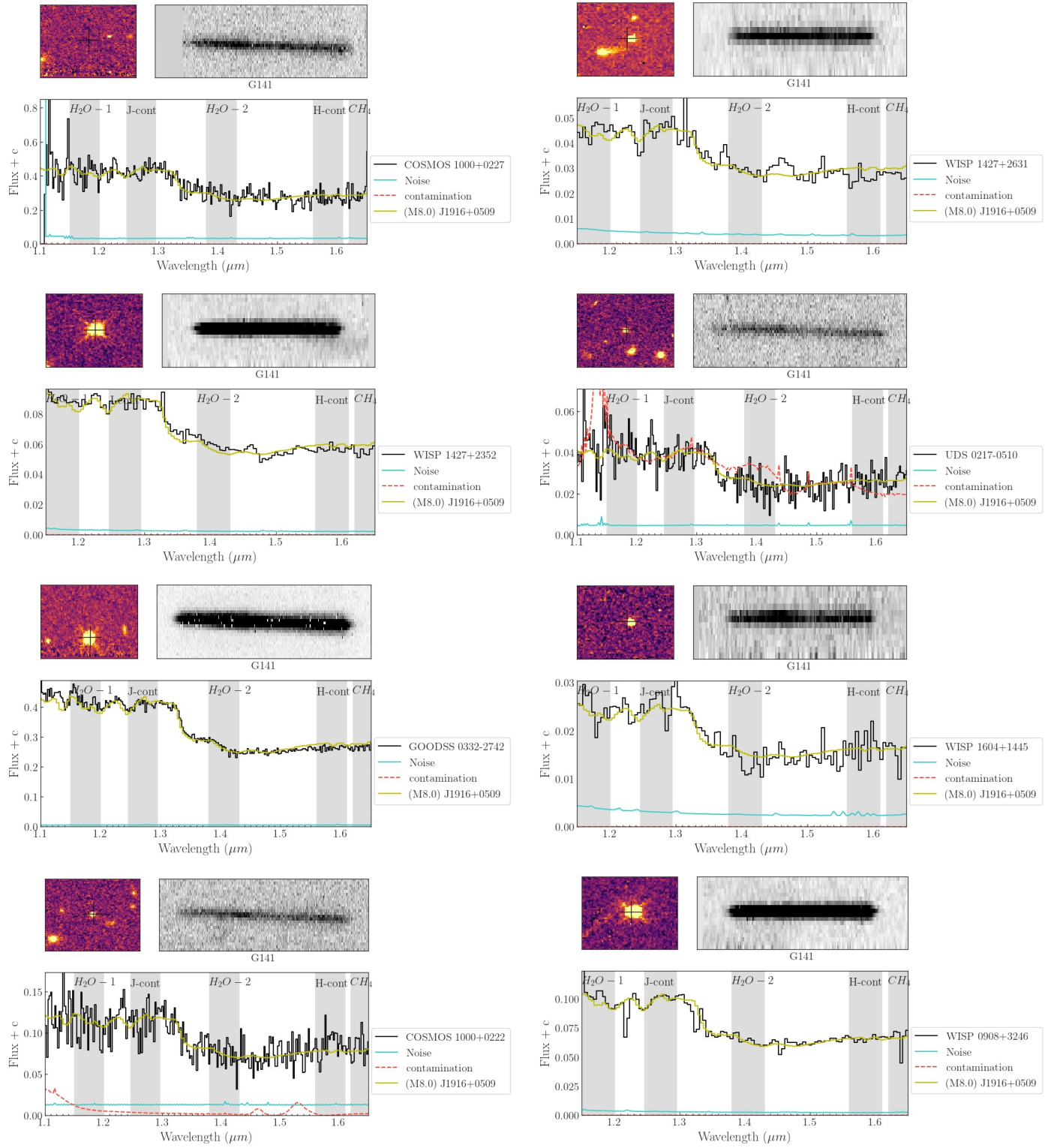
Figure 22. cont.

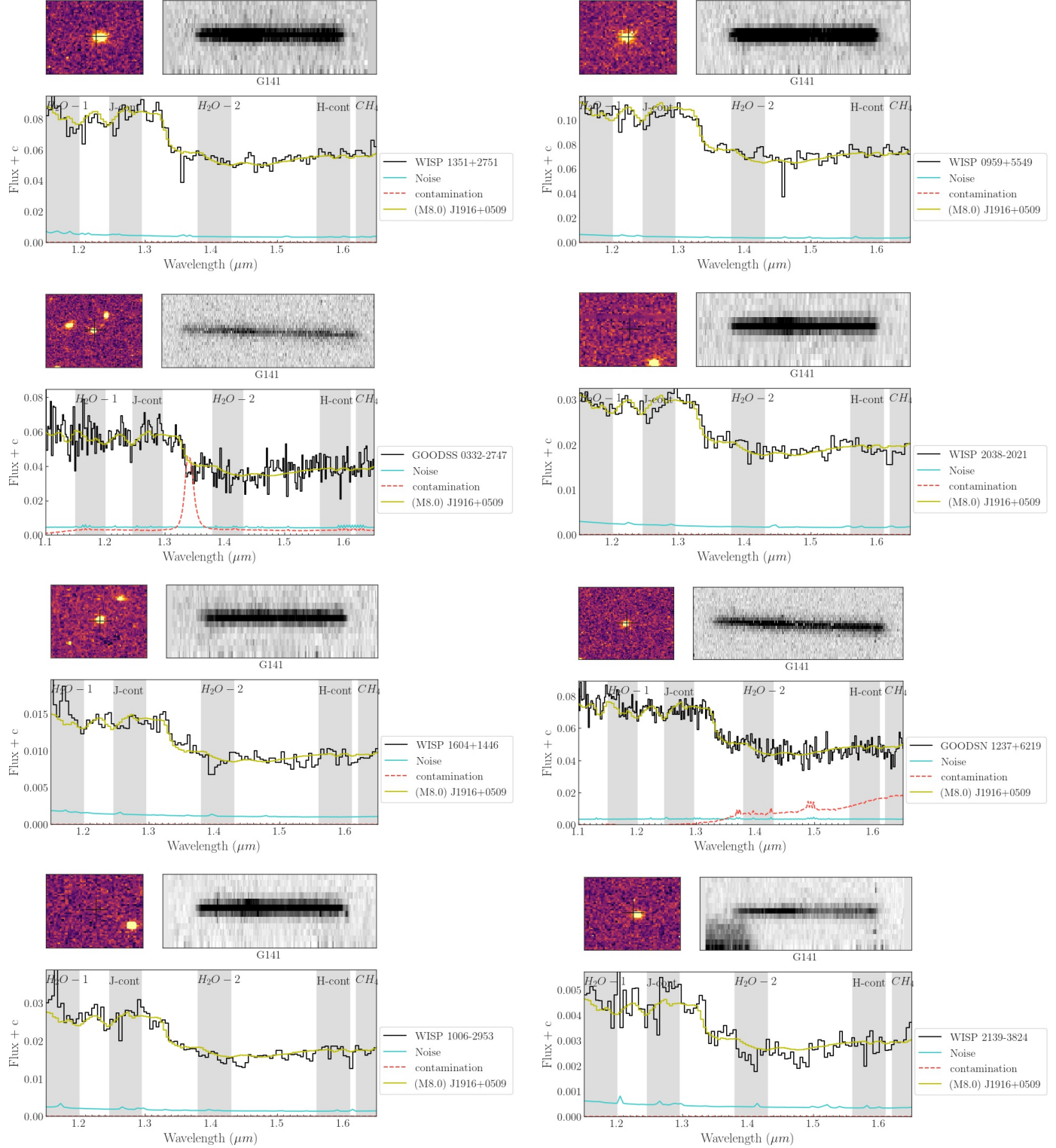
**Figure 23.** cont.

**Figure 24.** cont.

**Figure 25.** cont.

**Figure 26.** cont.

**Figure 27.** cont.

**Figure 28.** cont.

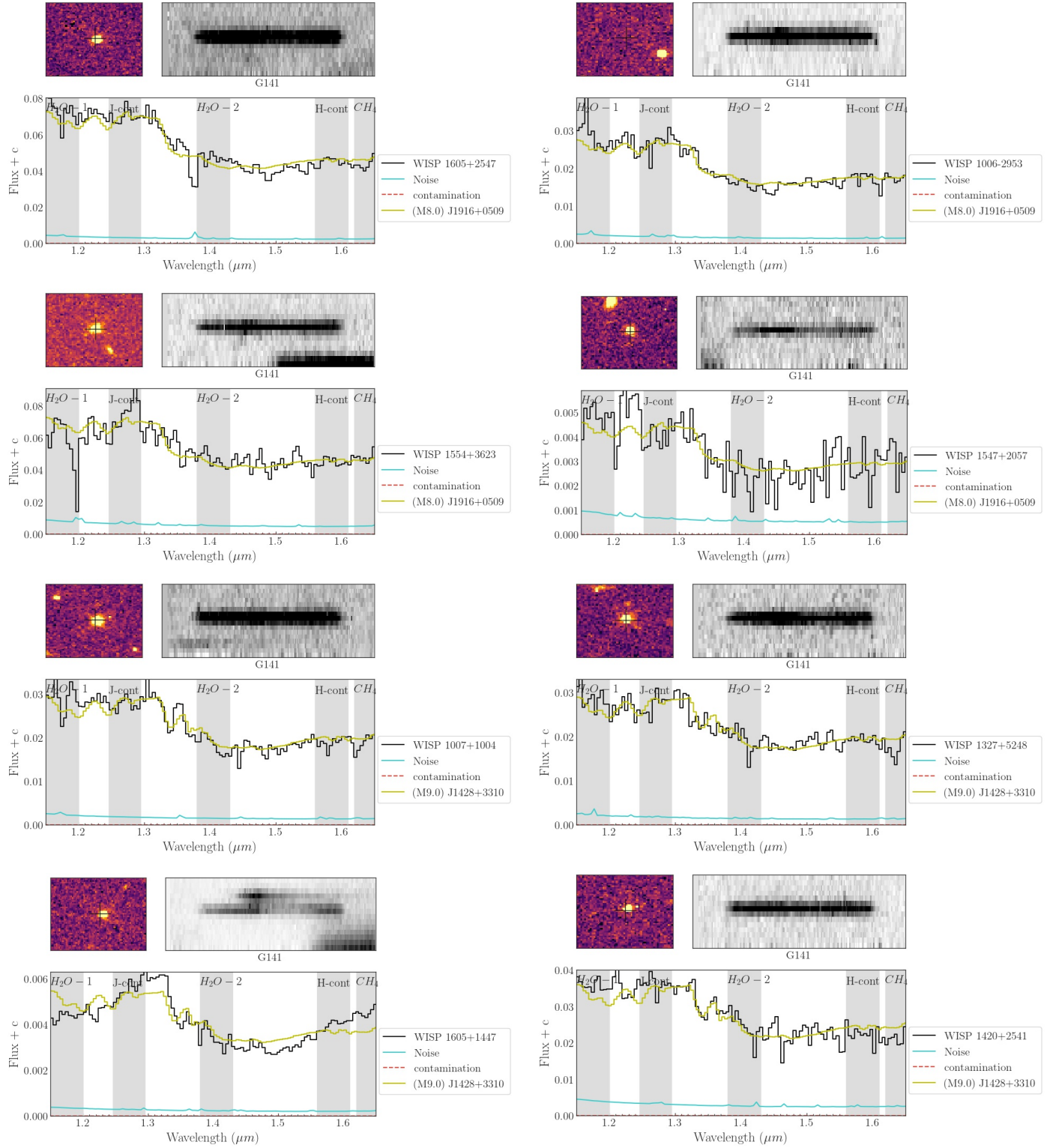


Figure 29. cont.

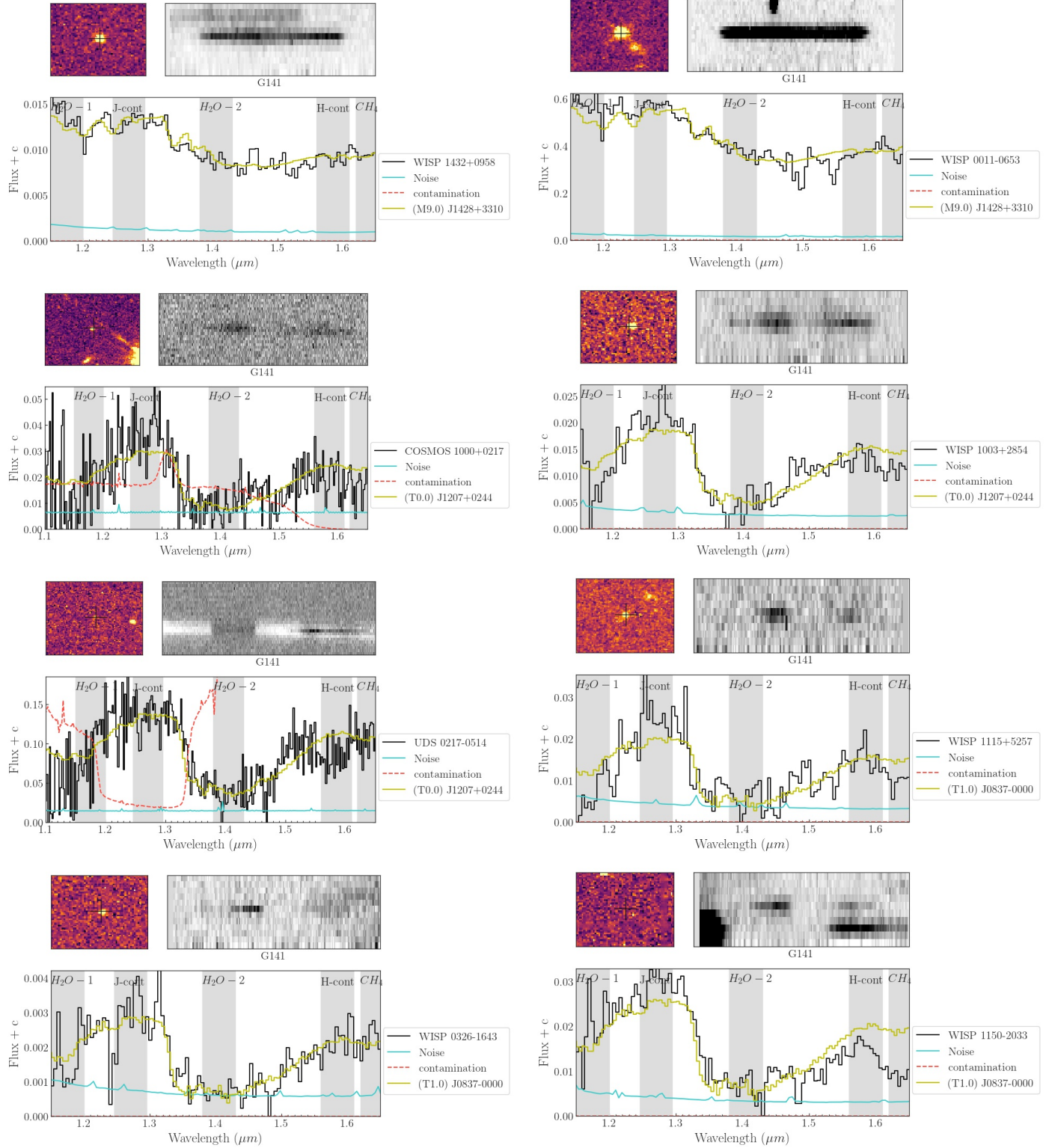
**Figure 30.** cont.

Table 1. Selection Criteria

SpT range	X-axis	Y-axis	v1	v2	v3	v4	CP	CT	FP
L0-L5	H ₂ O-1/J-Cont	H ₂ O-2/H ₂ O-1	(0.69, 0.84)	(0.98, 0.84)	(0.98, 0.46)	(0.69, 0.46)	0.97	0.075	0.93
L5-T0	H ₂ O-1/J-Cont	CH ₄ /H ₂ O-1	(0.51, 7.21)	(0.94, 7.21)	(0.94, -4.5)	(0.51, -4.5)	0.98	0.209	0.95
M7-L0	H ₂ O-1/J-Cont	CH ₄ /J-Cont	(0.83, 0.83)	(1.08, 0.83)	(1.08, 0.54)	(0.83, 0.54)	0.97	0.135	0.86
T0-T5	H ₂ O-1/J-Cont	CH ₄ /H-Cont	(0.23, 0.96)	(0.93, 1.74)	(0.93, 0.75)	(0.23, -0.04)	0.97	0.165	0.95
T5-T9	H-cont/H ₂ O-1	CH ₄ /J-Cont	(2.16, 0.24)	(12.39, 0.04)	(12.39, -0.14)	(2.16, 0.06)	0.95	0.001	0.71
Y dwarfs	CH ₄ /H ₂ O-1	H ₂ O-2/J-Cont	(-18.94, 0.15)	(12.03, 0.15)	(12.03, -0.17)	(-18.94, -0.17)	0.88	0.061	0.99
subdwarfs	H ₂ O-2/J-Cont	CH ₄ /H-Cont	(0.18, 1.17)	(0.75, 1.17)	(0.75, 0.86)	(0.18, 0.85)	0.89	0.163	0.91

Table 2. List of L0-T9 UCDs

ShortName	GrismID	SNR-J	SpT	RA	DEC	F110W	F140W	F160W	Distance(pc)	Distanceeir
WISP1007+1004	PAR343-00083	6	L0	151.936081	10.079100	23.0		22.4	2094	761
WISP1429+3224	PAR378-00052	8	L0	217.333206	32.416400	22.4		21.9	1661	651
WISP1715+0455	PAR239-00118	6	L0	258.758057	4.925150		22.1		1951	32
WISP2333+3925	PAR153-00002	518	L0	353.414642	39.418100			15.7	134	2
WISP1618+3340	PAR65-00035	19	L0	244.707458	33.671520	21.7		21.3	1225	518
WISP2333+3922	PAR68-00017	146	L0	353.398834	39.370580	18.7		18.7	351	171
WISP2307+2111	PAR166-00004	326	L0	346.827850	21.193400			16.6	199	3
WISP0246-0104	PAR483-00077	9	L0	41.721233	-1.079250	23.0		22.1	1903	591
WISP1408+5657	PAR353-00055	13	L1	212.082855	56.956800	22.5		22.0	1506	635
WISP1150-2033	PAR199-00009	57	L1	177.706833	-20.561000		19.2		449	10
WISP1700+2922	PAR137-00128	4	L1	255.171310	29.373300			23.3	3846	76
WISP0015-7955	PAR244-00072	6	L1	3.785810	-79.930220		22.2		1812	38
WISP1154+1941	PAR338-00035	13	L1	178.716644	19.684700	22.2		21.9	1436	662
WISP1133+0328	PAR27-00036	10	L2	173.274353	3.477643	21.6	22.0	21.4	1101	445
WISP1154+1939	PAR338-00136	4	L3	178.720154	19.660000	24.1		23.1	1877	693
WISP0927+6027	PAR21-00005	324	L4	141.989319	60.462970		18.6		196	6
WISP1004+5258	PAR438-00051	10	L4	151.204559	52.974800		22.6		1278	36
WISP0125-0001	PAR365-00156	4	L4	21.396976	-0.027310	5.6		24.2	1819	1820
WISP1625+5721	PAR156-00041	19	L4	246.353882	57.357600			21.4	982	26
WISP2322-3450	PAR368-00007	129	L5	350.663971	-34.841000	19.2		19.1	182	102
WISP2133-4904	PAR133-00012	87	L5	323.482574	-49.083000			19.6	362	9

Table 2 continued on next page

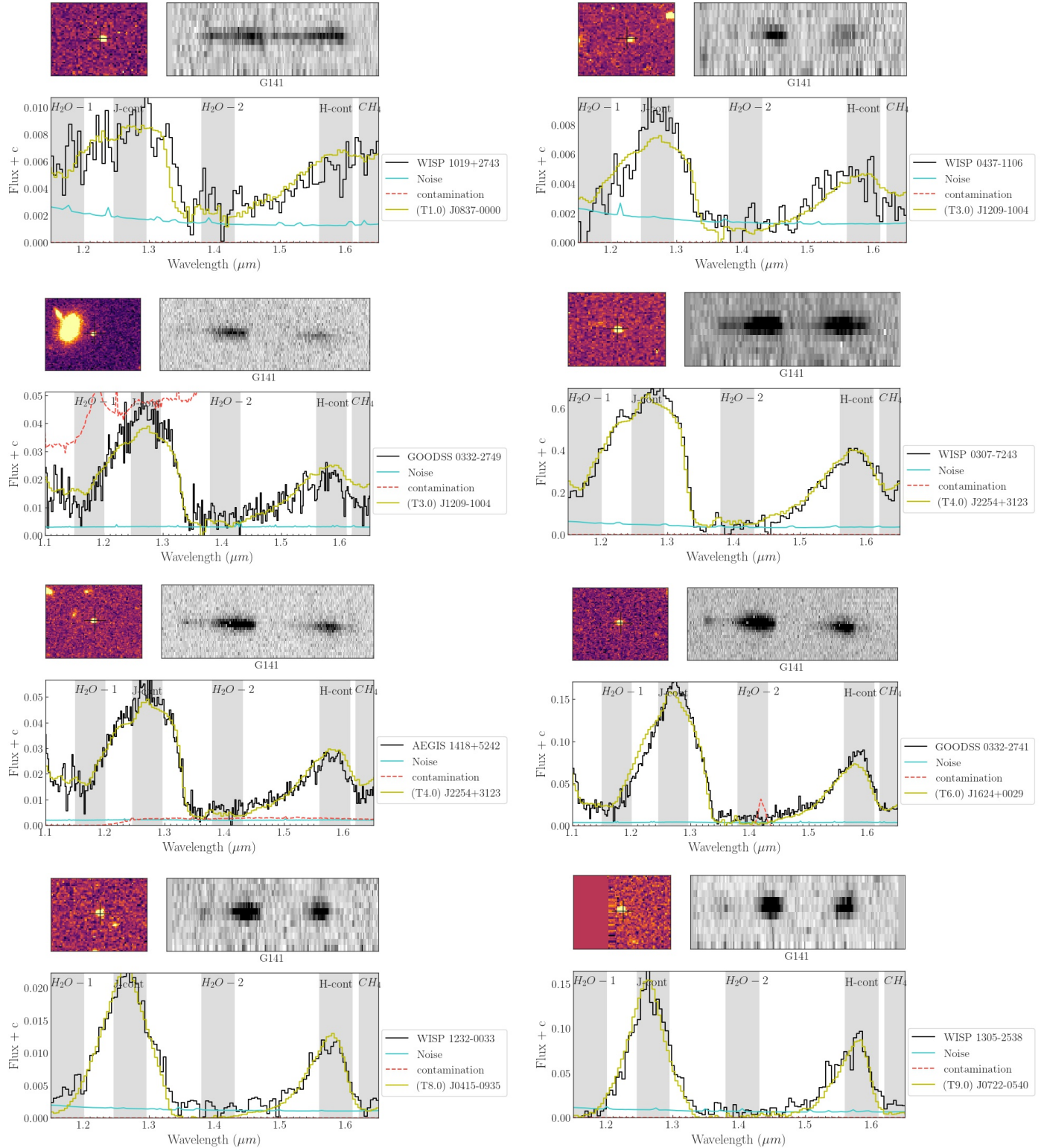
**Figure 31.** cont.**Table 2** continued on next page

Table 2 (*continued*)

ShortName	GrismID	SNR_J	SpT	RA	DEC	F110W	F140W	F160W	Distance(pc)	Distanceee
Table 2 (<i>continued</i>)										
ShortName	GrismID	SNR_J	SpT	RA	DEC	F110W	F140W	F160W	Distance(pc)	Distanceee
WISP1124+4202	PAR106-00047	11	L6	171.034760	42.042900			21.5	721	17
WISP0105+0215	PAR231-00012	89	L8	16.310194	2.257870		18.9		122	2
WISP1340+2823	PAR433-00004	258	L8	205.232132	28.399900	18.3		17.7	67	29
WISP1325+2233	PAR436-00037	20	M7	201.376205	22.555500	21.8		21.2	1685	393
WISP1348+2451	PAR243-00025	10	M7	207.047501	24.864700		21.7		2115	34
WISP0243-7211	PAR127-00028	33	M7	40.788712	-72.193700			20.7	1592	23
WISP1402+5410	PAR458-00004	107	M7	210.689911	54.173500	19.1		18.9	536	168
WISP0910+3328	PAR431-00028	11	M7	137.621338	33.466900	21.5		21.3	1648	517
WISP1023+0409	PAR347-00017	37	M7	155.843842	4.156480	20.7		20.5	1119	340
WISP2225-7212	PAR404-00044	15	M7	336.405060	-72.208000	21.9		21.7	1973	618
WISP1402+0946	PAR143-00045	11	M7	210.603149	9.769180	22.1		21.9	2135	642
WISP1847-6858	PAR134-00071	24	M7	281.901581	-68.969000			21.2	2018	30
WISP1832+5344	PAR124-00053	18	M7	278.104370	53.743200	21.9		21.8	2010	656
WISP1832+5345	PAR124-00065	13	M7	278.138306	53.753000	22.1		22.1	2311	788
WISP1342+1841	PAR139-00010	70	M7	205.607071	18.696800			20.2	1303	18
WISP1303+2952	PAR35-00023	43	M7	195.952576	29.867760	20.9	20.8	20.5	1255	274
WISP1046+1302	PAR116-00048	11	M7	161.706467	13.044400			22.2	3238	46
WISP1611+5221	PAR161-00061	11	M7	242.944473	52.355100			22.3	3456	50
WISP1354+1801	PAR361-00004	145	M7	208.564117	18.033100	18.5		19.0	508	219
WISP1540-0204	PAR446-00065	16	M7	235.006500	-2.077700	22.2		21.7	2066	503
WISP0950+3544	PAR192-00026	18	M7	147.742004	35.734600		21.5		1891	30
WISP1427+2631	PAR218-00032	13	M7	216.803177	26.519000		21.4		1849	29
WISP1009+3000	PAR39-00033	10	M7	152.409225	30.012280	21.7	22.0	21.1	1875	509
WISP1545+1155	PAR290-00009	76	M7	236.311707	11.916900		19.2		654	10
WISP2139-3824	PAR309-00023	29	M7	324.799408	-38.403000	21.2		20.9	1370	390
WISP1550+3959	PAR59-00072	13	M7	237.595795	39.991620		22.8		3426	54
WISP1419+0606	PAR345-00016	46	M7	214.868134	6.107460	20.8		20.7	1214	394
WISP0122-2837	PAR128-00034	16	M7	20.700928	-28.631500			21.9	2863	41
WISP1703+6136	PAR155-00040	22	M7	255.800537	61.614300			21.6	2503	35
WISP0948+1350	PAR427-00039	21	M7	147.228485	13.841600	22.4		22.1	2428	732
WISP0926+1239	PAR92-00011	27	M7	141.534668	12.664310			20.7	1642	24
WISP1437-0149	PAR66-00029	20	M7	219.364258	-1.828590	21.4		21.6	1754	685

Table 2 continued on next page

Table 2 (*continued*)

ShortName	GrismID	SNR_J	SpT	RA	DEC	F110W	F140W	F160W	Distance(pc)	Distancee ^{er}
WISP1007+5013	PAR98-00038	21	M7	151.942719	50.227020			21.5	2317	33
WISP1011-0447	PAR406-00062	11	M7	152.756714	-4.798300	22.5		22.4	2706	878
WISP1514+3617	PAR71-00034	10	M7	228.531723	36.291910	22.1		21.9	2156	661
WISP0944-1940	PAR293-00045	13	M7	146.159622	-19.679000		21.5		1932	31
WISP0944-1941	PAR293-00059	8	M7	146.153305	-19.696000		21.9		2369	38
WISP0914+4755	PAR299-00070	12	M7	138.669785	47.929800	22.7		22.4	2762	784
WISP1409+2621	PAR15-00041	12	M7	212.418945	26.350570	22.5	22.2	20.4	1958	512
WISP1534+1252	PAR457-00025	16	M7	233.733124	12.881000	21.5		21.6	1778	638
WISP1340+2825	PAR433-00047	14	M7	205.238373	28.421200	21.9		22.2	2315	950
WISP1256+5430	PAR110-00085	15	M7	194.249939	54.515200			22.4	3494	52
WISP1102+1053	PAR11-00046	11	M7	165.566360	10.897610	22.1	22.2	21.6	2240	511
WISP2040-0644	PAR248-00079	17	M7	310.109924	-6.737800		21.6		2039	33
WISP1427+2631	PAR218-00004	93	M7	216.788986	26.524500		18.3		431	7
WISP1005-2421	PAR336-00047	10	M7	151.336197	-24.362000	22.1		22.0	2258	756
WISP0947+5126	PAR478-00038	17	M7	146.750015	51.442600	22.3		21.6	2054	445
WISP0307-7245	PAR130-00076	8	M7	46.930344	-72.760500			22.4	3605	52
WISP2307+2112	PAR166-00044	15	M7	346.819458	21.202500			21.6	2457	35
WISP2005-4139	PAR371-00055	20	M7	301.420959	-41.655000	21.5		20.9	1480	323
WISP1545+0933	PAR138-00108	7	M7	236.393112	9.559070			22.8	4254	67
WISP2307+2112	PAR166-00041	17	M7	346.821686	21.208400			21.5	2380	33
WISP1305-2538	PAR32-00044	17	M7	196.330322	-25.638200	22.4	22.0	22.4	2550	746
WISP1230+8236	PAR228-00015	36	M7	187.697586	82.607900			20.2	1079	17
WISP2345+1510	PAR77-00045	12	M7	356.250092	15.176390			21.7	2554	37
WISP2345-4239	PAR356-00057	8	M8	356.253845	-42.658000	23.0		22.7	2776	947
WISP1125+5319	PAR477-00009	32	M8	171.342133	53.331300	20.8		20.4	993	339
WISP0718+7425	PAR103-00109	4	M8	109.619423	74.430300			23.3	4932	54
WISP0959+5549	PAR246-00017	21	M8	149.789856	55.820400		20.9		1339	15
WISP1604+1445	PAR240-00058	8	M8	241.243622	14.766600		22.4		2681	29
WISP1604+1446	PAR240-00051	10	M8	241.234528	14.782200		22.2		2480	28
WISP1023+0409	PAR347-00037	14	M8	155.843643	4.164820	22.2		22.0	1958	727
WISP1351+2751	PAR444-00034	16	M8	207.753510	27.852400	21.8		21.5	1586	566
WISP1224+6110	PAR422-00021	30	M8	186.109833	61.182500		21.4		1641	18
WISP2038-2021	PAR197-00054	12	M8	309.592621	-20.363000		21.1		1465	16
WISP2131-1202	PAR342-00050	6	M8	322.946167	-12.045000	22.9		22.6	2646	939

Table 2 continued on next page

Table 2 (*continued*)

ShortName	GrismID	SNR_J	SpT	RA	DEC	F110W	F140W	F160W	Distance(pc)	Distancearcsec
WISP1006-2953	PAR171-00081	13	M8	151.730759	-29.894000			21.9	2626	23
WISP1007+5012	PAR98-00082	7	M8	151.918472	50.205320			22.7	3800	36
WISP0911+1832	PAR271-00055	10	M8	137.887695	18.541900	22.2		21.8	1901	630
WISP0426+0505	PAR251-00034	10	M8	66.573364	5.089166		21.2		1510	16
WISP2139-3824	PAR309-00046	9	M8	324.795837	-38.402000	22.3		22.4	2277	957
WISP0839+6456	PAR250-00051	7	M8	129.813751	64.949100		22.3		2582	30
WISP1006-2953	PAR170-00081	13	M8	151.730759	-29.894000			21.9	2627	24
WISP1427+2352	PAR346-00021	29	M8	216.753586	23.878400	21.0		20.9	1191	484
WISP1605+2547	PAR148-00044	21	M8	241.354004	25.794100			21.9	2637	23
WISP0502+0732	PAR189-00077	7	M8	75.559814	7.535803		22.2		2486	28
WISP0137-0908	PAR317-00032	17	M8	24.328993	-9.148480	21.7		21.1	1413	432
WISP2335-3536	PAR359-00007	58	M8	353.832611	-35.602000	19.9		19.6	665	238
WISP0908+3246	PAR417-00014	30	M8	137.048172	32.776600	20.8		20.3	941	298
WISP0854+4351	PAR319-00085	7	M8	133.500824	43.853300	23.2		22.9	3055	1063
WISP1500+4127	PAR391-00011	33	M8	225.079330	41.457200	20.9		20.7	1106	413
WISP0122-2838	PAR128-00052	14	M8	20.687748	-28.646200			22.3	3155	28
WISP1112+3536	PAR44-00044	19	M8	168.058868	35.607950	21.6	22.2	21.6	1866	658
WISP1432+0958	PAR428-00062	9	M9	218.003204	9.968530	22.2		22.0	1815	749
WISP1227+4410	PAR224-00063	4	M9	186.987015	44.173400		22.6		2697	34
WISP1007+1004	PAR343-00036	15	M9	151.918076	10.079000	21.5		21.2	1288	528
WISP1605+1447	PAR240-00040	17	M9	241.256699	14.783400		22.0		2011	24
WISP1327+5248	PAR195-00023	14	M9	201.981293	52.809200		21.1		1323	16
WISP0011-0653	PAR261-00027	25	M9	2.953725	-6.896139	21.1		21.2	1214	565
WISP1003+2854	PAR191-00077	6	T0	150.918884	28.912800			23.1	942	14
WISP1115+5257	PAR468-00163	5	T1	168.809311	52.951400	24.3		24.4	1087	514
WISP1150-2033	PAR199-00124	6	T1	177.704559	-20.565000		23.2		683	8
WISP0326-1643	PAR467-00135	3	T1	51.511295	-16.722500	23.9		23.9	883	405
WISP1019+2743	PAR201-00044	4	T1	154.888565	27.720400		22.4		482	5
WISP0437-1106	PAR463-00176	4	T3	69.490608	-11.104400	24.3		24.3	865	301
WISP0307-7243	PAR130-00092	12	T4	46.921608	-72.732600			22.7	454	16
WISP1232-0033	PAR58-00112	11	T8	188.176712	-0.551850		23.1		136	9
WISP1305-2538	PAR32-00075	11	T9	196.356232	-25.641300	23.1	23.0	22.7	98	31

Table 3. Polynomial relations used in this work given by $y = \sum_{n=1}^7 c_n x^n$

x	y	Scatter	Coefficients						
			c7	c6	c5	c4	c3	c2	c1
SpT	AbsF110W	-2E-06	4E-04	-2.8E-02	1.	-20.	203.	-846.	
SpT	AbsF140W	1E-06	-3.4E05	-9.8E-04	1.5e-01	-5.	72.	-381	
SpT	AbsF160W		-1E-02	2.9E-01	-8.	98.	-485.		
F110W	logSNR-J	0.40				-0.02	0.64	-2.2	
F140W	logSNR-J	0.43				0.01	-0.8,	12	
F160W	logSNR-J	0.43				0.002	-0.38	8.4	

Table 4. Number Densities (N) and effective volumes (V in pc³) for each scale height in pc. Nobs is the number of UCDs in the sample

SpT	N_100	N_1000	N_250	N_275	N_300	N_325	N_350	N_obs	V_100	V_1000	V_250	V_275	V_300	V_325	V_350
M7	1142.8	81.1	95.5	93.8	51.5	51.7	48.9	65	983052	124965	79851	74370	71283	69738	69237
M8	225.3	54	43.7	45.3	26	27.1	26.4	29	193823	83208	36486	35905	35988	36518	37366
M9	59.1	38.6	22.7	24.6	14.6	15.6	15.5	5	50829	59507	19009	19475	20159	21003	21971
L0	19.7	28.5	13.1	14.6	8.8	9.6	9.8	5	16916	43862	10938	11541	12241	13023	13876
L1	8	20.5	8.1	9.2	5.7	6.4	6.6	4	6841	31585	6786	7334	7943	8610	9329
L2	3.8	13.9	5.4	6.2	3.9	4.4	4.7	3	3237	21386	4477	4943	5454	6004	6589
L3	2	8.8	3.7	4.4	2.8	3.2	3.4	0	1734	13509	3110	3490	3896	4323	4765
L4	1.2	5.3	2.7	3.2	2	2.3	2.4	8	1024	8146	2238	2526	2824	3126	3427
L5	0.8	3.2	2	2.3	1.5	1.7	1.7	3	656	4893	1639	1842	2044	2241	2430
L6	0.5	2	1.5	1.7	1.1	1.2	1.2	1	451	3064	1218	1356	1489	1614	1731
L7	0.4	1.3	1.1	1.3	0.8	0.9	0.9	0	332	2074	934	1030	1120	1202	1278
L8	0.3	1	0.9	1	0.6	0.7	0.7	2	262	1548	754	826	892	952	1006
L9	0.3	0.8	0.8	0.9	0.5	0.6	0.6	1	222	1274	649	708	761	810	853
T0	0.2	0.7	0.7	0.8	0.5	0.5	0.5	3	200	1132	591	643	690	733	770
T1	0.2	0.7	0.7	0.8	0.5	0.5	0.5	2	192	1042	557	605	648	686	720
T2	0.2	0.6	0.6	0.7	0.4	0.5	0.5	0	191	941	526	567	605	638	667
T3	0.2	0.5	0.6	0.6	0.4	0.4	0.4	1	192	786	475	508	536	562	584
T4	0.2	0.4	0.5	0.5	0.3	0.3	0.3	2	187	578	392	413	430	446	459
T5	0.2	0.2	0.3	0.4	0.2	0.2	0.2	0	162	361	278	288	296	303	309
T6	0.1	0.1	0.2	0.2	0.1	0.1	0.1	1	110	182	156	159	162	164	166
T7	0.1	0	0.1	0.1	0	0	0	0	49	66	61	61	62	62	63
T8	0	0	0	0	0	0	0	1	12	15	14	14	14	14	15
Total	1465.6	262.2	204.9	212.6	122.2	127.9	125.3	136	1260674	404124	171139	168604	169537	172772	177611

REFERENCES

Allers, K., Jaffe, D., Luhman, K., et al. 2007,
\apj, 657, 511

Antoja, T., Helmi, A., Romero-Gómez, M., et al.
2018, Nature, 561, 360

- Atek, H., Malkan, M., McCarthy, P., et al. 2010, *\apj*, 723, 104
- Aumer, M., & Binney, J. 2009, *\mnras*, 397, 1286
- Bahcall, J., & Soneira, R. 1981, *\apjs*, 47, 357
- Baraffe, I., Chabrier, G., Allard, F., & Hauschildt, P. 2003, in IAU Symposium, Vol. 211, Brown Dwarfs, ed. E. Martín, 41–+
- Bardalez Gagliuffi, D., Burgasser, A., Gelino, C., et al. 2014, *\apj*, 794, 143
- Bardalez Gagliuffi, D. C., Burgasser, A. J., Schmidt, S. J., et al. 2019, arXiv e-prints, arXiv:1906.04166
- Basri, G. 1998, in Astronomical Society of the Pacific Conference Series, Vol. 134, Brown Dwarfs and Extrasolar Planets, ed. R. Rebolo, E. Martin, & M. Zapatero Osorio, 394–+
- Bate, M., Bonnell, I., & Bromm, V. 2002, *\mnras*, 332, L65
- Bate, M., Bonnell, I., & Bromm, V. 2003, in Astronomical Society of the Pacific Conference Series, Vol. 287, Galactic Star Formation Across the Stellar Mass Spectrum, ed. J. De Buizer & N. van der Blieck, 427–432
- Belokurov, V., Erkal, D., Evans, N. W., Koposov, S. E., & Deason, A. J. 2018, *MNRAS*, 478, 611
- Bertin, E., & Arnouts, S. 1996, *\aaps*, 117, 393
- Bochanski, J., Hawley, S., Covey, K., et al. 2010, *\aj*, 139, 2679
- Boubert, D., Guillochon, J., Hawkins, K., et al. 2018, *MNRAS*, 479, 2789
- Boubert, D., Guillochon, J., Hawkins, K., et al. 2018, *Monthly Notices of the Royal Astronomical Society*, 479, 2789–2795
- Brammer, G., van Dokkum, P., Franx, M., et al. 2012a, *\apjs*, 200, 13
- Brammer, G. B., van Dokkum, P. G., Franx, M., et al. 2012b, *The Astrophysical Journal Supplement Series*, 200, 13
- Bromm, V., & Loeb, A. 2003, *Nature*, 425, 812
- Burgasser, A. 2001, PhD thesis, AA(Department of Physics, California Institute of Technology)
- . 2004, *\apjs*, 155, 191
- . 2007, *\apj*, 659, 655
- . 2014a, ArXiv e-prints, arXiv:1406.4887
- Burgasser, A.,Looper, D., Kirkpatrick, J., & Liu, M. 2007, *\apj*, 658, 557
- Burgasser, A. J. 2014b, arXiv:1406.4887
- Burningham, B., Cardoso, C., Smith, L., et al. 2013, *\mnras*, 433, 457
- Burrows, A., Hubbard, W., Lunine, J., & Liebert, J. 2001, *Reviews of Modern Physics*, 73, 719
- Carnero Rosell, A., Santiago, B., dal Ponte, M., et al. 2019, arXiv e-prints, arXiv:1903.10806
- Chabrier, G. 2001, *\apj*, 554, 1274
- Chabrier, G., & Baraffe, I. 2000, *\araa*, 38, 337
- Chabrier, G., & Mera, D. 1997, *A&A*, 328, 83
- Collaboration, T. A., Robitaille, T. P., Tollerud, E. J., et al. 2013, arXiv:1307.6212
- Cruz, K., Reid, I., Kirkpatrick, J., et al. 2007, *\aj*, 133, 439
- Cushing, M., Tokunaga, A., & Kobayashi, N. 2000, *\aj*, 119, 3019

- Cushing, M., Kirkpatrick, J., Gelino, C., et al. 2011, *\apj*, 743, 50
- Davis, M., Guhathakurta, P., Konidaris, N. P., et al. 2007, *The Astrophysical Journal Letters*, 660, L1
- Day-Jones, A., Marocco, F., Pinfield, D., et al. 2013, *\mnras*, 430, 1171
- de Vaucouleurs, G., & Pence, W. D. 1978, *AJ*, 83, 1163
- Delfosse, X., Tinney, C. G., Forveille, T., et al. 1999, *Astron. Astrophys. Suppl. Ser.*, 135, 41
- Downes, J. J., Briceño, C., Mateu, C., et al. 2014, *MNRAS*, 444, 1793
- Dupuy, T., & Liu, M. 2012, *\apjs*, 201, 19
- Faherty, J. K., Bochanski, J. J., Gagne, J., et al. 2018, *The Astrophysical Journal*, 863, 91
- Filippazzo, J. C., Rice, E. L., Faherty, J., et al. 2015, *Astrophysical Journal*, 810, 158
- Freeman, K. C. 1987, *ARA&A*, 25, 603
- Gagné, J., Faherty, J. K., Cruz, K. L., et al. 2015, *arXiv:1506.07712*
- Gaia Collaboration, Brown, A. G. A., Vallenari, A., et al. 2018, *A&A*, 616, A1
- Gallart, C., Bernard, E. J., Brook, C. B., et al. 2019, *Nature Astronomy*, doi:10.1038/s41550-019-0829-5
- Giavalisco, M., Ferguson, H. C., Koekemoer, A. M., et al. 2004, *The Astrophysical Journal*, 600, L93
- Gould, A., Bahcall, J., & Flynn, C. 1997, *\apj*, 482, 913
- Grogin, N. A., Kocevski, D. D., Faber, S. M., et al. 2011, *ApJS*, 197, 35
- Hardegree-Ullman, K. K., Cushing, M. C., Muirhead, P. S., & Christiansen, J. L. 2019, *arXiv e-prints*, arXiv:1905.05900
- Hayashi, C., & Nakano, T. 1963, *Progress of Theoretical Physics*, 30, 460
- Haywood, M., Di Matteo, P., Lehnert, M., Katz, D., & Gómez, A. 2013, *\aap*, 560, A109
- Helmi, A., Babusiaux, C., Koppelman, H. H., et al. 2018, *Nature*, 563, 85
- Holwerda, B. W., Trenti, M., Clarkson, W., et al. 2014, *The Astrophysical Journal*, 788, 77
- Hunter, J. D. 2007, *Computing in Science Engineering*, 9, 90
- Ivezić, Ž., Beers, T. C., & Jurić, M. 2012, *ARA&A*, 50, 251
- Jones, E., Oliphant, T., Peterson, P., et al. 2001–, SciPy: Open source scientific tools for Python, , [Online; accessed 1 today]
- Jurić, M., Ivezić, Ž., Brooks, A., et al. 2008, *\apj*, 673, 864
- Kerins, E. J. 1997, *A&A*, 328, 5
- Kiman, R., Schmidt, S. J., Angus, R., et al. 2019, *AJ*, 157, 231
- Kimble, R. A., MacKenty, J. W., O'Connell, R. W., & Townsend, J. A. 2008, *Wide Field Camera 3: a powerful new imager for the Hubble Space Telescope*, , doi:10.1117/12.789581
- Kirkpatrick, J. 2005, *\araa*, 43, 195

- Kirkpatrick, J., Looper, D., Burgasser, A., et al. 2010, *\apjs*, 190, 100
- Kirkpatrick, J., Cushing, M., Gelino, C., et al. 2011, *\apjs*, 197, 19
- Kirkpatrick, J. D., Reid, I. N., Liebert, J., et al. 2000, *The Astronomical Journal*, 120, 447
- Kirkpatrick, J. D., Martin, E. C., Smart, R. L., et al. 2019, *ApJS*, 240, 19
- Koekemoer, A. M., Faber, S. M., Ferguson, H. C., et al. 2011, *ApJS*, 197, 36
- Koppelman, H. H., Helmi, A., Massari, D., Price-Whelan, A. M., & Starkenburg, T. K. 2019, arXiv e-prints, arXiv:1909.08924
- Kümmel, M., Walsh, J. R., Pirzkal, N., Kuntschner, H., & Pasquali, A. 2009, *Publications of the Astronomical Society of the Pacific*, 121, 59
- Kuntschner, H., Kümmel, M., & Walsh, J. R. 2013
- Laughlin, G., Bodenheimer, P., & Adams, F. 1997, *\apj*, 482, 420
- Lawrence, A., & Others. 2007, *\mnras*, 379, 1599
- Leggett, S. K., Ruiz, M. T., & Bergeron, P. 1998, *ApJ*, 497, 294
- Lodieu, N., Espinoza Contreras, M., Zapatero Osorio, M. R., et al. 2017, *Astronomy & Astrophysics*, 598, A92
- Lodieu, N., Burningham, B., Day-Jones, A., et al. 2012, *A&A*, 548, A53
- Lopez-Santiago, J., Montes, D., Crespo-Chacon, I., & Fernandez-Figueroa, M. J. 2006, *The Astrophysical Journal*, 643, 1160
- LSST Science Collaboration, L. S., Abell, P. A., Allison, J., et al. 2009, arXiv:0912.0201
- Luhman, K. L., & Mamajek, E. E. 2012, *The Astrophysical Journal*, 758, 31
- Malhan, K., Ibata, R. A., & Martin, N. F. 2018, *MNRAS*, 481, 3442
- Mamajek, E. E. 2015, *Proceedings of the International Astronomical Union*, 10, 21
- Manjavacas, E., Apai, D., Zhou, Y., et al. 2018, arXiv:1812.03963
- Marocco, F., Jones, H. R. A., Day-Jones, A. C., et al. 2015, *Monthly Notices of the Royal Astronomical Society*, 449, 3651
- Martin, E. C., Mace, G. N., McLean, I. S., et al. 2017, *The Astrophysical Journal*, 838, 73
- Masters, D., McCarthy, P., Burgasser, A., et al. 2012, *\apjl*, 752, L14
- Metchev, S., Kirkpatrick, J., Berriman, G., & Looper, D. 2008, *\apj*, 676, 1281
- Miller, A. A., Kulkarni, M. K., Cao, Y., et al. 2017, *The Astronomical Journal*, 153, 73
- Momcheva, I. G., Brammer, G. B., van Dokkum, P. G., et al. 2016, *The Astrophysical Journal Supplement Series*, 225, 27
- Myeong, G. C., Evans, N. W., Belokurov, V., Sand ers, J. L., & Koposov, S. E. 2018, *ApJL*, 856, L26
- Myeong, G. C., Vasiliev, E., Iorio, G., Evans, N. W., & Belokurov, V. 2019, *MNRAS*, 488, 1235
- Pedregosa, F., Varoquaux, G., Gramfort, A., et al. 2012, arXiv e-prints, arXiv:1201.0490

- Pirzkal, N., Sahu, K., Burgasser, A., et al. 2005, \apj, 622, 319
- Pirzkal, N., Burgasser, A., Malhotra, S., et al. 2009, \apj, 695, 1591
- Reid, I., Kirkpatrick, J., Liebert, J., et al. 1999, \apj, 521, 613
- Reylé, C. 2018, Astronomy & Astrophysics, 619, L8
- Reyle, C., Delorme, P., Willott, C. J., et al. 2010, Astronomy and Astrophysics, Volume 522, id.A112, 15 pp., 522, arXiv:1008.2301
- Rujopakarn, W., Eisenstein, D. J., Rieke, G. H., et al. 2010, ApJ, 718, 1171
- Ryan, R. E., Thorman, P. A., Yan, H., et al. 2011, The Astrophysical Journal, 739, 83
- Ryan, R. E., Thorman, P. A., Schmidt, S. J., et al. 2017, The Astrophysical Journal, 847, 53
- Ryan Jr., R., Hathi, N., Cohen, S., & Windhorst, R. 2005, \apjl, 631, L159
- Ryan Jr., R. E., & Reid, I. N. 2016, The Astronomical Journal, 151, 92
- Salvatier, J., Wiecki, T. V., & Fonnesbeck, C. 2016, PeerJ Computer Science, 2, e55
- Schmidt, S., West, A., Bochanski, J., Hawley, S., & Kielty, C. 2014, \pasp, 126, 642
- Schmidt, S., West, A., Hawley, S., & Pineda, J. 2010, \aj, 139, 1808
- Schneider, A. C., Cushing, M. C., Kirkpatrick, J. D., et al. 2015, The Astrophysical Journal, 804, 92
- Scoville, N., Aussel, H., Brusa, M., et al. 2007, The Astrophysical Journal Supplement Series, 172, 1
- Skelton, R. E., Whitaker, K. E., Momcheva, I. G., et al. 2014, The Astrophysical Journal Supplement Series, 214, 24
- Skrzypek, N., Warren, S. J., & Faherty, J. K. 2016, A&A, 589, A49
- Sorahana, S., Nakajima, T., & Matsuoka, Y. 2018, arXiv:1811.07496
- Spergel, D., Gehrels, N., Baltay, C., et al. 2015, arXiv:1503.03757
- Theissen, C. A., West, A. A., Shippee, G., Burgasser, A. J., & Schmidt, S. J. 2017, AJ, 153, 92
- Tokunaga, A., & Kobayashi, N. 1999, \aj, 117, 1010
- Tolstoy, E., Hill, V., & Tosi, M. 2009, ARA&A, 47, 371
- Van Vledder, I., Van Der Vlugt, D., Holwerda, B. W., et al. 2016, Monthly Notices of the Royal Astronomical Society, 458, 425
- Virtanen, P., Gommers, R., Oliphant, T. E., et al. 2019, arXiv e-prints, arXiv:1907.10121
- Waskom, M., Botvinnik, O., Hobson, P., et al. 2014, seaborn: v0.5.0 (November 2014), v.v0.5.0, Zenodo, doi:10.5281/zenodo.12710
- York, D., & Others. 2000, \aj, 120, 1579